Epigenetic encoding of T cell dysfunction is enacted within hours of tumor antigen encounter prior to cell division

Mary Philip (mary.philip@vumc.org)
Vanderbilt University Medical Center https://orcid.org/0000-0001-7496-2630
Michael Rudloff
Vanderbilt University School of Medicine
Paul Zumbo
Weill Medical College, Cornell University
Natalie Favret
Vanderbilt University School of Medicine
Jessica Roetman
Vanderbilt University School of Medicine
Carlos Detres Roman
Vanderbilt University School of Medicine
Megan Erwin
Vanderbilt University School of Medicine https://orcid.org/0000-0002-7014-0856
Sriya Jonnakuti
Vanderbilt University School of Medicine
Friederike Dündar
Weill Cornell Medicine https://orcid.org/0000-0002-2301-112X
Doron Betel
Weill Cornell Medicine https://orcid.org/0000-0002-8006-7752

Article

Keywords:

Posted Date: August 30th, 2022

DOI: https://doi.org/10.21203/rs.3.rs-1927273/v1

TITLE

Epigenetic encoding of T cell dysfunction is enacted within hours of tumor antigen encounter prior to cell division

AUTHORS

Michael W. Rudloff[1], Paul Zumbo[2,3], Natalie R. Favret[1], Jessica J. Roetman[1], Carlos R. Detrés Román[1], Megan M. Erwin[1], Sriya T. Jonnakuti[1], Friederike Dündar[2,3], Doron Betel[3,4,5], Mary Philip[1,6,7]

AFFILIATIONS

[1]Department of Medicine, Division of Hematology and Oncology, Department of Pathology, Microbiology, and Immunology, Vanderbilt School of Medicine, Nashville, TN, USA.

[2]Department of Physiology and Biophysics, Weill Cornell Medicine, New York, NY, USA

[3]Applied Bioinformatics Core, Weill Cornell Medicine, New York, NY, USA

[4]Institute for Computational Biomedicine, Weill Cornell Medicine, New York, NY, USA.

[5]Division of Hematology and Medical Oncology, Department of Medicine, Weill Cornell Medicine, New York, NY USA.

[6]Vanderbilt Center for Immunobiology, Vanderbilt University Medical Center, Nashville, TN USA.

[7]Vanderbilt-Ingram Cancer Center, Vanderbilt University Medical Center, Nashville, TN, USA.

CORRESPONDENCE

mary.philip@vumc.org

SUMMARY

Tumor-specific CD8 T cells (TST) found in patients with cancer are unable to halt cancer progression. TST are dysfunctional and cannot produce effector cytokines or kill target cells[1]. TST dysfunction, also known as exhaustion, has been thought to be driven by chronic T cell receptor (TCR)/antigen stimulation over days to weeks, encoded by exhaustion/dysfunction-associated epigenetic and transcriptional programs[1,2]. However, we know little about (i) the interplay between CD8 T cell function and epigenetics during the initial hours after activation in both functional (acute infection) or dysfunctional contexts (tumors) or (ii) the kinetics of CD8 T cell effector or dysfunction differentiation and relationship to cell division. Nevertheless, is it widely thought that T cell effector differentiation requires cell division[3]. Here we tracked differentiation of naive antigen-specific CD8 T cells by cell division within the first hours (0-60 hours) after antigen activation in tumor-bearing hosts, comparing to T cells undergoing functional effector differentiation during acute infection (E). Surprisingly, while TST and E exhibited the same rapid activation and cell division kinetics, TST failed to acquire effector function and implemented exhaustion-associated chromatin features. Notably, epigenetic encoding of TST dysfunction began within 6 hours of antigen encounter, even prior to cell division. These findings not only challenge the paradigm that chronic T cell receptor stimulation drives dysfunction/exhaustion in tumors, but also refute for CD8 T cells the prevailing notion that cell division is required to initiate epigenetic remodeling and differentiation[3-7]. Interestingly, while T cell dysfunctional fate decisions are made within hours of antigen encounter, continued TCR stimulation and epigenetic remodeling progressively stabilize, or “imprint” the dysfunctional state. Our study defines for the first time the regulation and kinetics driving the rapid divergence of T cell fate choice prior to cell division in the context of tumors versus infection.

INTRODUCTION

CD8 T cell differentiation during acute infection has been well characterized: naive CD8 T cells encountering their cognate antigen are activated, begin rapidly proliferating, and acquire the ability to produce effector cytokines (IFNγ, TNFα) and cytolytic molecules (granzyme B; GZMB, perforin; PRF1)[8]. During chronic viral infection, CD8 T cells initially acquire effector function, but with persistent viral antigen stimulation over time, undergo gradual hierarchical loss of effector function and proliferative capacity, upregulate inhibitory receptors such as PD1 and LAG3, and become exhausted[2]. Tumor-specific CD8 T cells (TST) found in patients with cancer or in established murine tumors also lack effector function and express inhibitory receptors such as PD1 and LAG3; this dysfunction/exhaustion has been attributed to persistent tumor antigen exposure and the immunosuppressive microenvironment. However, the precise kinetics of how TST are activated, become dysfunctional, and first acquire epigenetic features of dysfunction/exhaustion is not known and has not been assessed *in vivo*.

In metazoans, proliferation and differentiation must be carefully regulated during embryogenesis and throughout life in order to ensure adequate cell numbers and organ function[9]. In immune cells such as developing thymocytes[7], helper T cells[3], and B cells[5,6], proliferation has been shown to be required for differentiation to proceed. During acute infection, 24 hours of antigen stimulation/priming is sufficient to set CD8 T cells on an antigen-independent proliferation and differentiation path to the functional effector and then memory states[10-12]. This phenomenon, known as CD8 T cell "autopilot" differentiation[13], suggests that the initial 24 hours after activation is a critical window in which CD8 T cell fate is determined. However, it is unknown whether a similar CD8 T cell autopilot differentiation occurs in tumors, driving T cells into a dysfunctional state.

To answer this question, we utilized our previously established autochthonous model of liver carcinogenesis, in which TST can be tracked longitudinally over hours, days, and weeks through the entire course of tumor development[14]. Using this model, we identified the critical features of tumor-induced CD8 T cell

dysfunction/exhaustion (reviewed in [1]), all of which have also been shown in human tumor-infiltrating lymphocytes (TIL)[15-19], including key transcription factor (TF) expression changes (loss of TCF1 and gain of TOX), upregulation of canonical inhibitory receptors (PD1, LAG3, CD39), and dysfunction/exhaustion-associated epigenetic and transcriptional hallmarks[18,19]. Therefore, we leveraged our ability to track TST cell division and differentiation with temporal precision in tumor-bearing hosts to determine (i) the kinetics and relationship between TST proliferation and dysfunction differentiation following antigen encounter in progressing tumors, (ii) transcriptional and chromatin state dynamics in TST in the critical window following activation during which functional/dysfunction fate selection occurs, and (iii) the temporal relationship between tumor antigen exposure, chromatin remodeling, and dysfunction "imprinting."

RESULTS

TST undergo robust proliferation but do not gain effector function

To determine the relationship between activation, proliferation, and differentiation to the functional or dysfunctional state, we labeled naive SV40 large T antigen (TAG)-specific CD8 T cells (TCR_{TAG}) with carboxyfluorescein succinimidyl ester (CFSE), which allows the tracking of cell divisions. CFSE-labeled TCR_{TAG} were adoptively transferred into mice with late-stage TAG-driven liver tumors (ASTxAlb-Cre), or into TAG-expressing *L. monocytogenes* (LM_{TAG})-infected C57BL/6 mice (B6). We reisolated and analyzed TCR_{TAG} 12, 36, 48, and 60 hours (h) after transfer to capture T cells at all stages of division (**Fig. 1a, b**). We observed remarkably similar robust cell division profiles for T cells in tumor-bearing (T) and infected hosts (E) (6+ divisions within 60h) and rapid induction of activation markers CD69 and CD44 (**Fig. 1b and Extended Data Fig. 1a, b**). Furthermore, both E-TCR_{TAG} and T-TCR_{TAG} upregulated LAG3 and PD1, indicating TCR signaling and activation[20,21] (**Fig. 1b and Extended Data Fig. 1a, b)**. T-TCR_{TAG} in tumors, liver draining lymph nodes (LDLN), and spleens of ASTxAlb-Cre hosts, underwent similar proliferation and immunophenotypic changes (**Extended Data Fig. 1a**). Surprisingly, despite proliferation kinetics identical to E-TCR_{TAG}, T-TCR_{TAG} failed to produce IFNγ and TNFα in response to TAG peptide restimulation *ex vivo*; this failure was observed as early as division

1 (**Fig. 1c, d and Extended Data Fig. 1c, d**). This was in sharp contrast to E-TCR_{TAG} from livers or spleens of infected mice, which robustly produced effector cytokines (IFNγ/TNFα) and cytolytic molecules (GZMB/PRF1) and were capable of degranulation (CD107a membrane localization) within a few cell divisions (**Fig. 1c, d and Extended Data Fig. 1c, d, e**). Thus, tumor antigen encounter drove CD8 T cell activation and proliferation as effectively as antigen presented during acute infection; however, in tumors, effector function (both cytokine and cytolytic effector arms) was not gained in conjunction with strong proliferation.

Tumor-induced TST dysfunction is established prior to cell division

Given that TST dysfunction was established within the first cell division, we next assessed differentiation during the first 18 hours prior to cell division (0, 6, 12, 18h) (**Fig. 2a and Extended Data Fig. 2a**). TCR_{TAG} in tumor-bearing mice were activated within 6h with similar kinetics as in infected mice, evidenced by CD69 induction and subsequent up-regulation of CD44, LAG3, and PD1 (**Fig. 2b and Extended Data Fig. 2a**). While E-TCR_{TAG} produced TNFα and rapidly gained IFNγ production capability, T-TCR_{TAG} showed cytokine impairment within 6h, with near total loss of cytokine production by 12h (**Fig. 2c, d**). T-TCR_{TAG} also failed to produce GZMB (**Fig. 2d and Extended Data Fig. 2b**). Thus, multiple arms of effector function were immediately silenced in TST. Interestingly, TOX, a DNA-binding protein we and others have previously shown to be associated with dysfunction in tumors and exhaustion in chronic viral infection[19,22-24], was not induced at these early timepoints (**Fig. 2e**), suggesting that TOX does not mediate the early loss of effector function.

To assess the contribution of inadequate priming to rapid dysfunction onset, we tested whether committed effector T cells would succumb to tumor-induced dysfunction with kinetics similar to naive T cells. We adoptively transferred CFSE-labeled day 5 effector TCR_{TAG} (E5d) from LM_{TAG}-infected B6 into tumor bearing ASTxAlb-Cre (E→T) or time matched LM_{TAG} infected B6 (E→E) and analyzed them 12h, 36h, and 7 days (d) later (**Extended Data Fig. 3a**). E→E remained IFNγ/TNFα double producers and re-expressed CD127 (IL7R) both in secondary recipient spleen (**Extended Data Fig. 3b, c, d**) and liver (data not shown), demonstrating that E5d

were committed functional effectors that underwent memory differentiation. In contrast, E→T proliferated after transfer but began losing cytokine production capacity within 12h with complete loss by 7d (**Extended Data Fig. 3b, c, d**). Remarkably, nearly all the effector function loss occurred prior to cell division in the secondary host (**Extended Data Fig. 3e, f**), demonstrating again that cell division is not needed for differentiation to the dysfunctional state. The rapid loss of cytokine function in committed effector CD8 T cells within 12 hours of transfer into tumor-bearing hosts suggests that inadequate priming was not the main driver of dysfunction. Our observation of cell division-independent induction of dysfunction in naive and effector T cells led us to ask whether dysfunction-associated epigenetic remodeling indeed requires cell division.

Dysfunction-associated epigenetic programming is enacted prior to cell division

We next sought to determine whether epigenetic and transcriptional changes encoding TST dysfunction were induced prior to cell division. We transferred CFSE-labeled TCR_{TAG} into late tumor-bearing ASTxAlb-Cre or LM_{TAG}-infected B6 mice, sorted T-TCR_{TAG} (from liver tumors at 6, 12, 24h) and E-TCR_{TAG} (from spleen at 6, 12, 24h), before they had undergone cell division (division 0), and assessed chromatin accessibility by Assay for Transposase-Accessible Chromatin with sequencing (ATAC-SEQ)[25] and gene expression by RNA-Sequencing (RNA-SEQ) (**Fig. 3a and Extended Data Fig. 4a**). Principle component analysis (PCA) of ATAC-SEQ and RNA-SEQ data showed that within just 6h, T- and E-TCR_{TAG} had distinct chromatin and gene expression profiles (PC2, **Fig. 3b and Extended Data Fig. 4b**). Strikingly, pre-division chromatin remodeling was mostly completed in the first 6h post-activation, with fewer changes occurring at 12 and 24h (**Fig. 3b, c**). 50% of differentially accessible chromatin peaks (DAC) were shared between T-(T6h) and E-TCR_{TAG} (E6h) (**Fig. 3d**) and included TCR signaling downstream genes (*Irf4*, *Nfatc2*, *Nfkb1*, *Lat*) and pathways (**Extended Data Fig. 4c**). Notably, there were a large number of DAC unique to T6h-TCR_{TAG} (35%), (**Fig. 3d**). *Pdcd1* contains an enhancer peak 23 kb upstream from the transcription start site (-23 kb) previously shown to drive *Pdcd1* expression in exhausted T cells during chronic viral infection[26]. Remarkably, we found that the -23kb "exhaustion"-associated *Pdcd1* peak was already uniquely accessible within 6h of T cell activation in tumors, but not during acute infection (**Extended**

Data Fig. 4d). Pathway analysis on the genes with the greatest changes in chromatin accessibility and expression in T6h-TCR_{TAG} relative to E6h-TCR_{TAG} revealed enrichment for negative regulatory pathways and genes (protein tyrosine/serine/threonine phosphatase activity*)* (**Fig. 3e**). RNA-SEQ analysis corroborated the chromatin accessibility data, showing that T-TCR_{TAG} induced greater expression of negative regulators of T cell function (*Rgs16, Pdcd1, Ptpn22*), and less expression of inflammatory associated genes (*Mx1, Isg15*), genes encoding cytokines/cytolytic mediators (*Ifng, Gzmb, Gzma*), and TF associated with functional differentiation (*Batf, Tbx21*)[27] relative to E-TCR_{TAG}. T-TCR_{TAG} expressed more *Bach2* and *Id3*, previously associated with memory phenotypes[28] and restraint of effector differentiation (**Fig. 3f**)[29]. In contrast, genes in inflammation-associated pathways (cellular response to type I interferon) were preferentially accessible (**Fig. 3e**) and expressed (**Fig. 3f**) in E6h-TCR_{TAG}, consistent with infection-induced innate immune activation. To identify potential TF driving chromatin remodeling, we performed motif analysis on DAC between E6h and T6h. Inflammation-induced TF family motifs such as IRF and STAT were enriched in E6h (**Extended Data Fig. 4e**), consistent with pathway analysis showing enrichment for inflammation-associated pathways (**Fig. 3e**). However, in TST, NFAT/AP1 TF family motifs were enriched in chromatin peaks opening in T6h (**Extended Data Fig. 4e**); thus, NFAT-driven transcription modules previously described for later T cell exhaustion/dysfunction[18,30], already commence within hours of tumor antigen encounter.

Pre-division tumor-induced TST chromatin remodeling is reinforced with time and tumor antigen exposure

We next examined whether early (6h) dysfunction-associated chromatin accessibility changes are maintained or evolve as TST undergo continued antigen exposure in progressing tumors. Therefore, we compared our 6-24h chromatin accessibility data with our previously published chromatin accessibility data from TCR_{TAG} isolated from liver tumors between 5-60d[18]. PCA showed that TST clustered into three groups based on the time of tumor exposure: early (6-12h), intermediate (5-7d), and late (14-60+d) (**Fig. 4a**). Strikingly, in assessing TST chromatin remodeling from 0h-60d, the largest number of changes occurred by 6h, with a second smaller round of peak

changes between 12h-5d, and a third round between 7-14d, after which very few changes occurred (**Fig. 4b upper, Extended Data Fig. 5a**). TCR_{TAG} in the setting of acute infection also had many early peak changes within 6h and a second round of peak changes between 24h and 5d. However, in contrast to TST in tumors that underwent a third wave of chromatin remodeling, likely driven by continued tumor antigen exposure, few peak changes occurred after E5d (**Fig. 4b lower, Extended Data Fig. 5a, b**), demonstrating that the memory-associated chromatin state was largely established early upon pathogen/antigen clearance.

We next compared how each individual chromatin peaks changed over time by plotting the fold-change of each peak's accessibility during the early transition (naive (N) to 6h) versus fold-change change during the intermediate (int) transition, (12h to 5d) (**Fig. 4c, d**). Thus, a peak in the "reinforced open" quadrant in the scheme in Fig. 4c had an increase in accessibility between N and 6h with a further increase in accessibility between 6h and 5d. In contrast, a peak in the "stable closed" quadrant had an early decrease in accessibility and remained "closed" during the later transition. This analysis revealed that nearly 60% of pre-division remodeled chromatin peaks in TST remained stable (28% closed, 31% open) with continued tumor antigen exposure and proliferation, with additional peaks getting reinforced (int 4%) (**Fig. 4c, d and Extended Data Fig. 5c top)**. This was in marked contrast with differentiation during infection, in which many early chromatin accessibility changes were transient (35%) or newly occurred between 24h and 5d (int 39%) (**Fig. 4c,d and Extended Data Fig. 5c lower**). The *Pdcd1* locus exemplifies these patterns, with peak changes maintained and reinforced with time in tumors and transient during acute infection-induced effector/memory differentiation (**Fig. 4e, f**), consistent with its transient surface expression (Extended Data Fig. 1a). The -23kb *Pdcd1* enhancer peak, which opens within 6h in TST but not in T cells responding to infection, had increased accessibility over time in tumors (**Fig. 4e**).

Duration of tumor antigen exposure determines dysfunction stability and imprinting

Given that we observed dysfunction-associated chromatin remodeling and loss of effector function within 6h of tumor antigen encounter, we next asked about the stability or "imprinting" of early tumor-induced dysfunction.

Would TST removed from the tumor and transferred to tumor-free hosts continue on "autopilot" as dysfunctional T cells? To address this, TCR_{TAG} were re-isolated from liver tumors after 1, 5, or 10 days (T1d, T5d, and T10d) and transferred into tumor-free B6 mice (T1d→B6, T5d→B6, T10d→B6) (**Fig. 5a**). Prior to transfer, tumor-activated TCR_{TAG} failed to make cytokine (**Fig. 5b**). After 5 days of parking, T1d→B6 uniformly downregulated PD1 (**Fig. 5c**), yet ~35-40% remained dysfunctional and were unable to produce TNFα or IFNγ (**Fig. 5b, d**). With longer primary tumor exposure, more TCR_{TAG} had "imprinted" dysfunction, with nearly all T10d→B6 failing to make effector cytokine and also retaining PD1 expression (**Fig. 5b, c**). In contrast, TOX expression was uniformly lost after TST removal from tumor, even after 10d tumor exposure, (**Fig. 5c, d**), suggesting that TOX expression is dependent on antigen/TCR stimulation or requires even longer tumor exposure to become imprinted. In line with this, analysis of chromatin accessibility changes within the *Tox* locus chromatin in TST revealed that multiple chromatin peaks were newly opened or closed during the int (T5-7d) to late (T14-60d) transition (**Extended Data Fig. 5d, e**). Taken together, our data demonstrate that CD8 T cells encountering tumor antigen undergo rapid chromatin remodeling before cell division, exhibiting canonical exhaustion/dysfunction hallmarks previously associated with later stages of differentiation. While some dysfunction hallmarks were imprinted within hours (loss of cytotoxic function), other features, such PD1 and TOX expression, required additional days of tumor antigen exposure and further locus chromatin remodeling to become imprinted.

DISCUSSION

Here, we describe for the first time the functional, immunophenotypic, epigenetic, and transcriptional features of TST differentiating cell division by cell division within the hours following tumor antigen encounter *in vivo*. Though TST were activated and proliferated rapidly and identically to CD8 T cells during acute infection, TST in tumor-bearing hosts lost/failed to gain both effector cytokine and cytolytic function. Remarkably, this dysfunction was evident even prior to cell division. Rapid loss of effector function *in vivo* coincided with extensive chromatin remodeling and transcriptional alterations in TST, including chromatin peak accessibility changes previously characterized as "exhaustion-associated." These findings upend the previous paradigm that

tumor-induced T cell dysfunction occurs through persistent antigen stimulation over days to weeks and instead show that CD8 T cell integrate multiple signaling inputs (TCR, co-stimulatory/inhibitory, and cytokine) immediately following activation in different contexts, which dictate their differentiation to the functional effector fate (infection) or the dysfunction fate (tumors).

Proliferation and differentiation are intimately connected throughout development[9], and previous studies showed that proliferation was required for the epigenetic remodeling associated with differentiation for thymocytes and other adaptive immune lineages[4-7]. However, we find that CD8 T cells execute large scale chromatin remodeling and differentiation prior to undergoing cell division. This begs the question whether and why CD8 T cell epigenetic remodeling and differentiation kinetics differ from CD4 T cell or B cell differentiation. As our study is the first to examine adaptive immune cell differentiation and chromatin remodeling during the first hours following activation *in vivo* prior to cell division, it remains to be seen whether CD4 T cells similarly undergo early rapid differentiation to the functional or dysfunctional state, as such studies have not been done. A previous study of human polyclonal CD4 T cell activation *in vitro* using anti-CD3/CD28 stimulation found early extensive chromatin remodeling[31]. Further studies will be needed to determine whether CD8 and CD4 T cell differentiation and epigenetic remodeling after activation *in vivo* share similar kinetics and features. Nevertheless, despite dramatic effector function loss, dysfunctional TST proliferated as rapidly and robustly as T cells during acute infection; thus, the regulation of proliferation and functional effector differentiation is uncoupled. This finding, in line with previous studies *in vitro* or in self-tolerance models[32,33], has important implications for cancer immunotherapy, as efforts aimed at boosting TST proliferation by gene targeting may not be sufficient to reverse effector function loss[34-36].

While the initial decision to differentiate to the functional or dysfunctional state was made rapidly prior to cell division, TST proliferated and underwent additional chromatin remodeling with time and antigen exposure that stabilized and even reinforced initial dysfunction epigenetic programs. These findings together with our previous

work[18,19] demonstrate that the T cell dysfunctional state is composed of different modules (loss of effector function, upregulation of inhibitory receptors, proliferative capacity), which are regulated independently. This was borne out when we tested the degree to which early TST dysfunction was "imprinted"—that is retained upon removal from the tumor and transfer into tumor-free hosts. Loss of effector function, one of the earliest events during dysfunctional differentiation, is imprinted in a large fraction of dysfunctional TST after only brief tumor exposure, while PD1 expression requires more prolonged tumor exposure and epigenetic reinforcement to become fixed. Interestingly, expression of TOX, a key dysfunction-associated TF, was not imprinted even after 10d of tumor exposure, suggesting that TOX expression is dependent on antigen/TCR stimulation or requires even longer tumor exposure to become imprinted. Indeed, recent studies showed that later exhausted T cells (>30d exposure) from humans and murine models of chronic viral infection retained TOX expression and exhaustion-associated chromatin peaks after transfer to antigen-free hosts or viral cure with direct acting anti-viral therapy[37-39].

Given how rapidly CD8 T cells differentiate to the dysfunctional state in tumor-bearing hosts, with early epigenetic remodeling further reinforced over time/tumor progression, in order to improve T cell-based cancer immunotherapy, we need to target both early dysfunction induction as well as dysfunction reinforcement. Further studies are needed to understand how CD8 T cells rapidly integrate TCR and context-dependent inputs to make fate choices. Only by deciphering the complex network of signaling and gene regulatory networks that lie between TCR and context-dependent inputs and fate choice outputs, can we design strategies to alter or redirect T cells into functional cancer killers.

FIGURE LEGENDS

Figure 1| TST undergo robust proliferation but do not gain effector function. a, Experimental scheme: CFSE-labeled naive TCR_{TAG} (Thy1.1) were adoptively transferred into B6 (Thy1.2), LM_{TAG}-infected B6 (Thy1.2), or ASTxAlb-Cre mice (Thy1.2) bearing late-stage liver tumors. TCR_{TAG} were re-isolated at 12, 36, 48, and 60 hours (h) from infected spleen or tumor livers for flow cytometric analysis (Naive *in vivo* (N; grey); Effector (E; green);

Tumor (T; blue)). **b**, TCR_{TAG} CFSE dilution assessed at each timepoint (upper) with CD44 and LAG3 versus CFSE dilution at all timepoints (lower) shown in comparison to N. All flow plots are gated on live $CD8^+$ $Thy1.1^+$ TCR_{TAG}, and data for each timepoint is concatenated from 3-4 biologic replicates. **c**, TCR_{TAG} IFNγ and TNFα production after 4h *ex vivo* TAG peptide stimulation, assessed by flow cytometry. Inset numbers represent percent of population in each gate. Gates were set based on no stimulation controls. **d**, Percentage of $IFN\gamma^+TNF\alpha^+$ and $CD107a^+$ $CD8^+$ $Thy1.1^+$ TCR_{TAG} (E48/60h and T48/60h) following *ex vivo* TAG peptide stimulation, and granzyme B (GZMB) and perforin (PRF1) expression immediately *ex vivo.* Each symbol represents an individual mouse. $^{**}P<0.01$, $^{****}P<0.0001$ determined using unpaired two-tailed Student's t-test. Experiments were repeated three times with n=3-4 for infection and tumor-bearing mice groups.

Figure 2| Tumor-induced TST dysfunction is established prior to cell division. a, Experimental scheme: CFSE-labeled naive TCR_{TAG} (Thy1.1) were adoptively transferred into B6 (Thy1.2), LM_{TAG}-infected B6 (Thy1.2), or ASTxAlb-Cre mice (Thy1.2) bearing late-stage liver tumors, and lymphocytes were re-isolated from tumor livers (blue) and infected spleens (green) at 6, 12, and 18h post-transfer for analysis by flow cytometry. **b**, Live $CD8^+$ $Thy1.1^+$ TCR_{TAG} CFSE dilution at each timepoint (left) and histogram and summary plot of CD69 expression (right) shown in comparison to naive *in vivo* (N; grey). **c**, TCR_{TAG} intracellular IFNγ and TNFα production after 4h *ex vivo* TAG peptide stimulation, with inset numbers indicating percentage of cells in each gate. Gates set based on no stim controls. **d**, Summary plots of TNFαIFNγ double-positive and *ex* vivo GZMB expression in TCR_{TAG}. Each symbol represents an individual mouse. **e**, Histograms and summary plots of TOX expression. $CD8^+$ $CD90.1^-$ $PD1^{hi}$ endogenous (endo) dysfunctional T cells are shown as the positive control for TOX staining. Histograms show representative data of group. $^{**}P<0.01$, $^{****}P<0.0001$ determined by two-way ANOVA with post hoc Tukey test. Experiments were repeated twice with n=3-4 mice per group.

Figure 3| Dysfunction-associated epigenetic reprogramming is enacted prior to cell division. a, Experimental scheme. CFSE-labeled naive TCR_{TAG} (Thy1.1) were adoptively transferred into LM_{TAG}-infected B6 (Thy1.2), or

ASTxAlb-Cre mice (Thy1.2) bearing late-stage liver tumors, and lymphocytes were flow-sorted from spleens and livers at 6, 12, and 24h post-transfer. **b**, Principal component analysis (PCA) comparing peak accessibility of naive (N; grey), and TCR_{TAG} differentiating during acute infection (green) and in tumors (blue) at 6, 12, and 24h post-transfer. Each symbol represents a single biological replicate. **c**, Number of chromatin accessibility peak changes during each transition (opening peaks, red; closing peaks, blue; *FDR*<0.05). **d**, Chromatin accessibility heatmap. Each row represents one of 19,763 differentially accessible peaks (*FDR*<0.05, |Log2FC| >1) displayed over 2kb window centered on the peak summit. Scale units are reads per genomic content (RPGC) normalized to 1x sequencing depth for 20 bp bins with blue indicating closed chromatin and red open chromatin. Peaks are ordered by membership within each subset shown in the Venn diagram (right) and hierarchical-clustering within the subset. Venn diagram showing quantity of differentially accessible chromatin peaks (DAC) that are unique to T cells in infection, unique to T cells in tumors, or shared between T cells in infection and tumors. **e,** Combined chromatin accessibility and differential gene expression analysis of TCR_{TAG} in tumor livers relative to infected spleens at 6h timepoint. Upper panel shows 50 most differentially-expressed genes (*FDR*< 0.05, |Log2FC| >1) with at least one DAC (*FDR*< 0.05). Each row of diamonds (left) corresponds to one gene and shows opening (red), unchanged (grey), and closed (blue) DAC. Circles (right) indicate corresponding gene expression (upregulated in red, downregulated in blue). Lower panel shows Gene ontology analysis performed on all DEG with at least one DAC in TCR_{TAG} in tumors relative to infection at 6h (113 genes up; 266 down). **f,** Heatmap showing differential gene expression between TCR_{TAG} in tumor versus infection at 6h from selected pathways (adjusted *P* <0.05, $|Log_2FC| >1$), z-score normalization across rows.

Figure 4| Pre-division tumor-induced TST chromatin remodeling is reinforced with time and tumor antigen exposure. a, PCA of chromatin accessibility of naive TCR_{TAG} (N) and after 6, 12h (early), 5d, 7d (intermediate; int), 14d, 21d, 28d, 35d, and 60d+ (late) in liver tumors. **b**, Number of chromatin accessibility peak changes during CD8 T cell differentiation in tumors (upper) and infection (lower) across each transition (opening peaks, red; closing peaks, blue) *FDR*<0.05). **c**, Legend corresponding to part d identifying chromatin accessibility

peak quadrants in scatterplots of early transition peak accessibility changes (x-axis) versus later transition peak changes (y-axis)**. d,** Upper panel shows chromatin peak accessibility changes during naive (N) → early (T6h) transition (log2FC T6h/N) versus early → int (T5d) transition (log2FC T5d/T12h). Lower panel shows chromatin peak accessibility changes during N→ early (E6h) transition (log2FC E6h/N) versus early → int (E5d) transition (log2FC E5d/E24h). Each point represents an individual DAC peak colored according to the legend in c. To the right are shown corresponding bar plots showing the number of chromatin peaks in each quadrant with opening peaks above the axis and closing peaks below the axis (includes DAC with adjusted $P<0.05$ for either comparison). **e**, Chromatin accessibility profile across the *Pdcd1* locus for TCR_{TAG} differentiating during infection and in liver tumors. Boxes highlight differentially accessible peaks in tumor and/or infection colored as in c. The exhaustion-associated -23kb enhancer peak in *Pdcd1* is highlighted in light orange denoting a chromatin peak whose opening is reinforced during tumor progression. Light purple boxes highlight transiently closed and open peaks found in TCR_{TAG} during infection, while for TCR_{TAG} in tumors, the dark purple box highlights a peak that opens and is maintained at later timepoints, and the dark orange boxes highlight peaks that open early and increase in accessibility at later timepoints. **f**, Scatterplot highlighting individual *Pdcd1* peaks (red) in TCR_{TAG} in tumors and infected mice relative to the overall pattern of chromatin peak changes (grey).

Figure 5| Duration of tumor antigen exposure determines dysfunction stability and imprinting. a, Experimental scheme: TCR_{TAG} activated in tumors for 1, 5, or 10d were isolated from tumors, transferred to tumor-free B6 mice, parked for 5d, and then isolated from secondary hosts and analyzed. **b,** Live $CD8^+$ $Thy1.1^+$ TCR_{TAG} analyzed *ex vivo* from tumors (upper) and after 5d parking (lower). TNFα and IFNγ production was measured following 4h *ex vivo* TAG peptide stim. Inset numbers represent percentage of population within each gate. Gates set based on no peptide stimulation controls. **c,** Histogram plots of *ex vivo* tumor activated TCR_{TAG} (blue) and concatenated post-parking samples (purple), with naive (N; grey) for comparison. TCR_{TAG} activated in tumors for 1d (upper), 5d (middle), and 10d (lower). **d,** Summary plots show the percentage positive for TNFα, IFNγ, PD1, and TOX *ex vivo* (for pooled donor TCR_{TAG} from 3-4 mice) and following 5d parking. *$P<0.05$,

**P<0.01, ***P<0.001, ****P<0.0001, ns=not significant, determined for change from baseline by one sample Student's t-test. Experiments were repeated twice with n=3-4 mice per group.

ACKNOWLEDGEMENTS

We thank A. Schietinger and members of the Philip laboratory for helpful discussions. We thank G. Anzarova and T. Bryson for technical assistance. We thank the Vanderbilt Division of Animal Care, D. Flaherty and the Vanderbilt University Medical Center Flow (VUMC) Cytometry Shared Resource Core, A. Jones and the Vanderbilt Technologies for Advanced Genomics (VANTAGE) Core, and A. Viale and the Sloan Kettering Integrated Genomics Operation Core (IGO). We thank P. Lauer and Aduro Biotech for providing attenuated *Listeria* strains. We thank J.C. Rathmell and J.M. Balko for critical review of the manuscript. This work was supported by the following funding sources: Medical Scientist Training Program (MSTP) NIH T32GM007347 to the Vanderbilt MSTP Program (M.W.R.), V Foundation Scholar Award (M.P.), NIH R37CA263614 (M.P.), Serodino Family Adventure Allee Fund (M.P.), Vanderbilt-Ingram Cancer Center (VICC) SPORE Career Enhancement Program (M.P.) NIH P50CA098131, Vanderbilt Digestive Disease Research Center (VDDRC) Young Investigator and Pilot Award (M.P.) NIH P30DK058404, NIH T32GM008554 (N.R.F.), NIH T32CA009592 (C.R.D.R), and NIH T32AR059039 (M.M.E.). The VUMC Flow Cytometry Shared Resource is supported by the VICC (NIH P30CA68485) and the VDDRC (NIH P30DK058404). VANTAGE is supported by the VICC (NIH P30CA68485), the Vanderbilt Vision Center (NIH P30EY08126) and the NIH G20RR030956. IGO is supported by NIH P30CA08748, Cycle for Survival, and the Marie-Josée and Henry R. Kravis Center for Molecular Oncology.

AUTHOR CONTRIBUTIONS

M.W.R and M.P. conceived and designed the study and analyzed and interpreted data. M.W.R. carried out experiments, assisted by N.R.F., J.J.R., C.R.D.R, M.M.E, and S.T.J. P.Z., F.D., and D.B. designed and performed

computational analyses of RNA-SEQ and ATAC-SEQ data. M.W.R. and M.P. wrote the manuscript, with all authors contributing to the writing and providing feedback.

REFERENCES

1 Philip, M. & Schietinger, A. CD8(+) T cell differentiation and dysfunction in cancer. Nat Rev Immunol 22, 209-223, doi:10.1038/s41577-021-00574-3 (2022).
2 McLane, L. M., Abdel-Hakeem, M. S. & Wherry, E. J. CD8 T Cell Exhaustion During Chronic Viral Infection and Cancer. Annu Rev Immunol, doi:10.1146/annurev-immunol-041015-055318 (2019).
3 Murphy, K. M., Weaver, C. A. & Berg, L. J. Janeway's Immunobiology. 10th edn, 38 (2022).
4 Bird, J. J. et al. Helper T cell differentiation is controlled by the cell cycle. Immunity 9, 229-237 (1998).
5 Tangye, S. G. & Hodgkin, P. D. Divide and conquer: the importance of cell division in regulating B-cell responses. Immunology 112, 509-520, doi:10.1111/j.1365-2567.2004.01950.x (2004).
6 Scharer, C. D., Barwick, B. G., Guo, M., Bally, A. P. R. & Boss, J. M. Plasma cell differentiation is controlled by multiple cell division-coupled epigenetic programs. Nature communications 9, 1698, doi:10.1038/s41467-018-04125-8 (2018).
7 Kreslavsky, T. et al. beta-Selection-Induced Proliferation Is Required for alphabeta T Cell Differentiation. Immunity 37, 840-853, doi:10.1016/j.immuni.2012.08.020 (2012).
8 Williams, M. A. & Bevan, M. J. Effector and memory CTL differentiation. Annu Rev Immunol 25, 171-192, doi:10.1146/annurev.immunol.25.022106.141548 (2007).
9 Zhu, L. & Skoultchi, A. I. Coordinating cell proliferation and differentiation. Curr Opin Genet Dev 11, 91-97, doi:10.1016/s0959-437x(00)00162-3 (2001).
10 Kaech, S. M. & Ahmed, R. Memory CD8+ T cell differentiation: initial antigen encounter triggers a developmental program in naive cells. Nat Immunol 2, 415-422, doi:10.1038/87720 (2001).
11 van Stipdonk, M. J., Lemmens, E. E. & Schoenberger, S. P. Naive CTLs require a single brief period of antigenic stimulation for clonal expansion and differentiation. Nat Immunol 2, 423-429, doi:10.1038/87730 (2001).
12 Williams, M. A. & Bevan, M. J. Shortening the infectious period does not alter expansion of CD8 T cells but diminishes their capacity to differentiate into memory cells. Journal of immunology 173, 6694-6702, doi:10.4049/jimmunol.173.11.6694 (2004).
13 Bevan, M. J. & Fink, P. J. The CD8 response on autopilot. Nat Immunol 2, 381-382, doi:10.1038/87676 (2001).
14 Schietinger, A. et al. Tumor-Specific T Cell Dysfunction Is a Dynamic Antigen-Driven Differentiation Program Initiated Early during Tumorigenesis. Immunity 45, 389-401, doi:10.1016/j.immuni.2016.07.011 (2016).
15 Minnie, S. A. et al. Myeloma escape after stem cell transplantation is a consequence of T-cell exhaustion and is prevented by TIGIT blockade. Blood 132, 1675-1688, doi:10.1182/blood-2018-01-825240 (2018).
16 Li, H. et al. Dysfunctional CD8 T Cells Form a Proliferative, Dynamically Regulated Compartment within Human Melanoma. Cell 176, 775-789 e718, doi:10.1016/j.cell.2018.11.043 (2019).
17 Yost, K. E. et al. Clonal replacement of tumor-specific T cells following PD-1 blockade. Nat Med 25, 1251-1259, doi:10.1038/s41591-019-0522-3 (2019).
18 Philip, M. et al. Chromatin states define tumour-specific T cell dysfunction and reprogramming. Nature 545, 452-456, doi:10.1038/nature22367 (2017).
19 Scott, A. C. et al. TOX is a critical regulator of tumour-specific T cell differentiation. Nature 571, 270-274, doi:10.1038/s41586-019-1324-y (2019).
20 Okazaki, T. et al. PD-1 and LAG-3 inhibitory co-receptors act synergistically to prevent autoimmunity in mice. J Exp Med 208, 395-407, doi:10.1084/jem.20100466 (2011).
21 Ahn, E. et al. Role of PD-1 during effector CD8 T cell differentiation. Proc Natl Acad Sci U S A 115, 4749-4754, doi:10.1073/pnas.1718217115 (2018).
22 Alfei, F. et al. TOX reinforces the phenotype and longevity of exhausted T cells in chronic viral infection. Nature 571, 265-269, doi:10.1038/s41586-019-1326-9 (2019).

23 Khan, O. et al. TOX transcriptionally and epigenetically programs CD8(+) T cell exhaustion. Nature, doi:10.1038/s41586-019-1325-x (2019).
24 Yao, C. et al. Single-cell RNA-seq reveals TOX as a key regulator of CD8(+) T cell persistence in chronic infection. Nat Immunol 20, 890-901, doi:10.1038/s41590-019-0403-4 (2019).
25 Buenrostro, J. D., Giresi, P. G., Zaba, L. C., Chang, H. Y. & Greenleaf, W. J. Transposition of native chromatin for fast and sensitive epigenomic profiling of open chromatin, DNA-binding proteins and nucleosome position. Nature methods 10, 1213-1218, doi:10.1038/nmeth.2688 (2013).
26 Sen, D. R. et al. The epigenetic landscape of T cell exhaustion. Science 354, 1165-1169, doi:10.1126/science.aae0491 (2016).
27 Tsao, H. W. et al. Batf-mediated epigenetic control of effector CD8(+) T cell differentiation. Sci Immunol 7, eabi4919, doi:10.1126/sciimmunol.abi4919 (2022).
28 Yang, C. Y. et al. The transcriptional regulators Id2 and Id3 control the formation of distinct memory CD8+ T cell subsets. Nat Immunol 12, 1221-1229, doi:10.1038/ni.2158 (2011).
29 Roychoudhuri, R. et al. BACH2 regulates CD8 T cell differentiation by controlling access of AP-1 factors to enhancers. Nat Immunol, doi:10.1038/ni.3441 (2016).
30 Martinez, G. J. et al. The transcription factor NFAT promotes exhaustion of activated CD8(+) T cells. Immunity 42, 265-278, doi:10.1016/j.immuni.2015.01.006 (2015).
31 Yukawa, M. et al. AP-1 activity induced by co-stimulation is required for chromatin opening during T cell activation. J Exp Med 217, doi:10.1084/jem.20182009 (2020).
32 Hernandez, J., Aung, S., Marquardt, K. & Sherman, L. A. Uncoupling of proliferative potential and gain of effector function by CD8(+) T cells responding to self-antigens. J Exp Med 196, 323-333, doi:10.1084/jem.20011612 (2002).
33 Curtsinger, J. M., Lins, D. C. & Mescher, M. F. Signal 3 determines tolerance versus full activation of naive CD8 T cells: dissociating proliferation and development of effector function. J Exp Med 197, 1141-1151, doi:10.1084/jem.20021910 (2003).
34 Belk, J. A. et al. Genome-wide CRISPR screens of T cell exhaustion identify chromatin remodeling factors that limit T cell persistence. Cancer Cell 40, 768-786 e767, doi:10.1016/j.ccell.2022.06.001 (2022).
35 Guo, A. et al. cBAF complex components and MYC cooperate early in CD8(+) T cell fate. Nature 607, 135-141, doi:10.1038/s41586-022-04849-0 (2022).
36 Legut, M. et al. A genome-scale screen for synthetic drivers of T cell proliferation. Nature 603, 728-735, doi:10.1038/s41586-022-04494-7 (2022).
37 Abdel-Hakeem, M. S. et al. Epigenetic scarring of exhausted T cells hinders memory differentiation upon eliminating chronic antigenic stimulation. Nat Immunol 22, 1008-1019, doi:10.1038/s41590-021-00975-5 (2021).
38 Hensel, N. et al. Memory-like HCV-specific CD8(+) T cells retain a molecular scar after cure of chronic HCV infection. Nat Immunol 22, 229-239, doi:10.1038/s41590-020-00817-w (2021).
39 Yates, K. B. et al. Epigenetic scars of CD8(+) T cell exhaustion persist after cure of chronic infection in humans. Nat Immunol 22, 1020-1029, doi:10.1038/s41590-021-00979-1 (2021).

METHODS

Mice. TCR_{TAG} transgenic mice (B6.Cg-Tg(TcraY1,TcrbY1)416Tev/J)[40], Alb-Cre (B6.Cg-Tg(Alb-cre)21Mgn/J), and C57BL/6J Thy1.1 mice were purchased from The Jackson Laboratory. TCR_{TAG};Thy1.1 double transgenic mice were generated by crossing Thy1.1 mice to TCR_{TAG} mice. ASTxAlb-Cre[14] double transgenic mice were generated by crossing AST (Albumin-floxStop-SV40 large T antigen (TAG))[41] with Alb-Cre mice. Both female and male mice were used for studies. T cell donor mice were between 6-10 weeks of age and sex-matched to recipient male and female C57BL/6 and ASTxAlb-Cre recipients. All mice were bred and housed in the animal facility at Vanderbilt University Medical Center (VUMC). All animal experiments were performed in compliance with VUMC Institutional Animal Care and Use Committee (IACUC) regulations.

Adoptive T cell transfer in acute infection and tumor models. C57BL/6 mice were inoculated i.v. with $5x10^6$ CFU *Listeria monocytogenes* (Lm) Δ*actA* Δ*inlB* strain[42] expressing the TAG-I epitope (SAINNYAQKL, SV40 large T antigen 206–215) (Aduro Biotech) 6-12h prior to T cell adoptive transfer for generation of effectors. Spleens from naive TCR_{TAG};Thy1.1 mice were mechanically disrupted with the back of 3 mL syringe and filtered through a 70 mm strainer into ammonium chloride potassium (ACK) buffer to lyse erythrocytes. Cells were washed twice with cold serum-free RPMI 1640 media and $2.5x10^6$ TCR_{TAG};Thy1.1 $CD8^+$ T cells were adoptively transferred into C57BL/6 (Thy1.2) mice inoculated with LM_{TAG} or ASTxAlb-Cre tumor bearing mice. For CFSE labeling studies, splenocytes were resuspended after first wash in 2.5 mL of plain, serum-free RPMI 1640, rapidly mixed with equal volumes of 2x CFSE [10μM] solution, incubated for 5 min at 37°C at a final CFSE [5 μM], quenched by mixing CFSE/cell solution with equal volume of pure FBS, washed twice with serum-free RPMI, and resuspended in serum-free RPMI for transfer.

Cell isolation for subsequent analyses. Spleens from experimental mice were mechanically disrupted with the back of 3 mL syringe and filtered through a 70 μm strainer into ACK buffer. Cells were washed once and resuspended in cold RPMI 1640 supplemented with 2 μM glutamine, 100 U/mL penicillin/streptomycin, and 10%

FBS (cRPMI). Liver tissue was mechanically disrupted using a 150 μm metal mesh and glass pestle in ice-cold 2% FBS/PBS and passed through a 70 μm strainer. Liver homogenate was centrifuged at 400g for 5 min at 4°C and supernatant discarded. Liver pellet was resuspended in 20 mL of 2% FBS/PBS buffer containing 500 U heparin, mixed with 13 mL of Percoll (GE) by inversion, and centrifuged at 500g for 10 min at 4°C. Supernatant was discarded and pellet was RBC lysed in ACK buffer and resuspended in cRPMI for downstream applications. Periportal and celiac lymph nodes were collected and pooled for tumor draining lymph node analysis. Lymph nodes were mechanically dissociated into single cell solutions using the textured surface of two frosted microscope slides into ice-cold cRPMI.

Intracellular cytokine staining and transcription factor staining. Intracellular cytokine staining was performed with the Foxp3/Transcription Factor Staining Buffer Kit (Tonbo) per manufacturer's instructions. Briefly, T cells were mixed with $2x10^6$ C57BL/6 splenocytes and stimulated with 0.5 μg/mL of TAG epitope I peptide in cRPMI for 4 hours at 37°C in the presence of brefeldin A (BioLegend). Where indicated, stim media contained anti-CD107a antibody. Following peptide stimulation, cells were stained with for surface markers, fixed, permeabilized, and stained for IFNγ, TNFα, perforin, and granzyme B. Intracellular transcription factor staining was performed with the Foxp3/Transcription Factor Staining Buffer Kit (Tonbo) per manufacturer's instructions

Flow cytometry and flow sorting. All flow analysis was performed on the Attune NXT Acoustic Focusing Cytometer (ThermoFisher Scientific). Data was analyzed using FlowJo v.10.8.1 (Tree Star Inc.). Cell sorting was performed using the BD FACS Aria III (BD Biosciences) at the VUMC Flow Cytometry Shared Resource Core with BD FACSDiva Software.

RNA sequencing (RNA-SEQ). ACK lysed single cell suspensions from livers and spleens were processed as described above using sterile technique and stained with antibodies against CD8, CD90.1, and CD69 and (4',6-

diamidino-2-phenylindole) DAPI for dead cell exclusion. 5,000 cells were sorted directly into Trizol LS and frozen. Total RNA was extracted from sorted cells using the Rneasy Micro kit (Qiagen) and amplified using the SMART-Seq v4 UltraLow Input RNA Kit (Clontech). The cDNA was quantified and analyzed on the BioAnalyzer. Libraries were prepared using 7.7-300 ng of cDNA and the NEB DNA Ultra II kit. Each library was quantitated post PCR and run on the Caliper GX to assess each library profile. A final quality control assay consisting of qPCR was completed for each sample. The libraries were sequenced using the NovaSeq 6000 with 150 bp paired end reads targeting 50M reads per sample. RTA (version 2.4.11; Illumina) was used for base calling and analysis was completed using MultiQC v1.7.5.

ATAC sequencing (ATAC-SEQ). Profiling of chromatin was performed by ATAC-seq as previously described[25]. ACK lysed single cell suspensions from livers and spleens were processed as described above using sterile technique and stained with antibodies against CD8, CD90.1, and CD69 and (4',6-diamidino-2-phenylindole) DAPI for dead cell exclusion. 15-20,000 cells were sorted into cold FCS, DMSO added to 10%, and cells frozen. Frozen T cells were then thawed and washed in cold PBS and lysed. The transposition reaction was incubated at 42°C for 45 min. The DNA was cleaned with the MinElute PCR Purification Kit (Qiagen), and material was amplified for five cycles. After evaluation by real-time PCR, 7–13 additional PCR cycles were done. The final product was cleaned by AMPure XP beads (Beckman Coulter) at a 1× ratio, and size selection was performed at a 0.5× ratio. Libraries were sequenced on a HiSeq 2500 or HiSeq 4000 in a 50-bp/50-bp paired-end run using the TruSeq SBS Kit v4, HiSeq Rapid SBS Kit v2, or HiSeq 3000/4000 SBS Kit (Illumina).

Statistical analyses. Statistical analyses on flow cytometric data were performed as described in the figure legends using Prism 9.0 software (GraphPad Software).

Bioinformatics methods. The quality of the sequenced reads was assessed with FastQC[43] and QoRTs[44] (for RNA-seq samples). Unless otherwise stated, plots involving high-throughput sequencing data were created using R v4.1.0[45] and ggplot2[46]. Code has been deposited in GitHub: https://github.com/abcwcm/Rudloff2022.

RNA-SEQ data analysis. Adaptors were trimmed from raw sequencing reads with TrimGalore v0.5.0 (http://www.bioinformatics.babraham.ac.uk/projects/trim_galore/) and Cutadapt v2.8[47]. Trimmed reads were mapped with STAR v2.7.6a[48] to the mouse reference genome (GRCm38.p6). Fragments per gene were counted with featureCounts v2.0.7[49] with respect to Gencode vM25 comprehensive gene annotations. Differentially expressed genes were identified by Wald tests using DESeq2 v1.32.0[50], and only Benjamini–Hochberg corrected *P* values < 0.05 were considered statistically significant.

Principial component analysis and expression heatmaps were created using variance-stabilizing transformed counts generated by the DESeq2 package. Heatmaps are centered and scaled by row.

ATAC-SEQ data

Alignment and identification of open chromatin regions

Reads were aligned to the mouse reference genome (GRCm38) with BWA-backtrack[51]. Post alignment filtering was done with samtools v1.8[52] and Broad Institute's Picard tools (http://broadinstitute.github.io/picard/) to remove unmapped reads, improperly paired reads, nonunique reads, and duplicates. To identify regions of open chromatin, peak calling was performed with MACS2 v2.2.7.1[53]. Only peaks with adjusted *P* values smaller than 0.01 were retained.

ATAC-SEQ peak atlas creation

Consensus peak sets were generated for tumor and infection at each transition if a peak was found in at least two replicates. Reproducible peaks at each transition were merged with DiffBind v3.2.1[54] to create an atlas of

accessible peaks, which was used for downstream analyses. The peak atlas was annotated using the ChIPseeker v1.30.0[55] and TxDb.Mmusculus.UCSC.mm10.knownGene[56].

Differentially accessible regions

Regions where the chromatin accessibility changed between different conditions were identified with DESeq2 v1.32.0, and only Benjamini–Hochberg corrected *P* values < 0.05 were considered statistically significant. A $\log_2$fold change cutoff of 1 was used in some analyses as indicated. When comparing earlier time points against previously published chromatin accessibility data at later time points, hidden batch effects were estimated using the svaseq function from sva v3.40.0[57], and the top 3 surrogate variables were accounted for in DESeq2.

Motif analysis

Peaks were analyzed for transcription factor (TF) motif enrichment using chromVAR v1.14.0[58]. Motifs from the CIS-BP database[59] ('mouse_pwms_v2' from chromVARmotifs v0.2.0) were used as input, after removing TFs that were lowly expressed based on the RNA-SEQ data (average count-per-million < 10). TF accessibility deviation scores and variability were calculated by chromVAR, and z-scores of deviations of the top 25 most variable TFs were visualized in a heatmap.

Peak heatmaps and genome coverage plots

Genome coverage files per replicate were normalized for differences in sequencing depth (RPGC normalization) with bamCoverage from deepTools v3.1.0[60]. Blacklisted regions were excluded (https://sites.google.com/site/anshulkundaje/projects/blacklists). Replicates were averaged together using UCSC-tools bigWigMerge and by dividing by the number of samples. ATAC-SEQ heatmaps were created using profileplyr v1.8.0[61] and ComplexHeatmap v2.8.0[62], by binning the region +/− 1kb around the peak summits in 20bp bins. To improve visibility, bins with read counts greater than the 75th percentile + 1.5*IQR were capped at that value.

Pathway analysis. Gene ontology pathway enrichment was performed on selected genes as described in figure legends using the web-based tool Enrichr[63].

Data availability. All data generated and supporting the findings of this study are available within the paper. The RNA-SEQ and ATAC-SEQ data have been deposited in the Gene Expression Omnibus (GEO Super-Series accession number GSE209712).

METHODS REFERENCES

40 Staveley-O'Carroll, K. *et al.* In vivo ligation of CD40 enhances priming against the endogenous tumor antigen and promotes CD8+ T cell effector function in SV40 T antigen transgenic mice. *Journal of immunology* **171**, 697-707 (2003).

41 Stahl, S. *et al.* Tumor agonist peptides break tolerance and elicit effective CTL responses in an inducible mouse model of hepatocellular carcinoma. *Immunol Lett* **123**, 31-37, doi:10.1016/j.imlet.2009.01.011 (2009).

42 Brockstedt, D. G. *et al.* Listeria-based cancer vaccines that segregate immunogenicity from toxicity. *Proc Natl Acad Sci U S A* **101**, 13832-13837, doi:10.1073/pnas.0406035101 (2004).

43 Andrews, S. FastQC: a quality control tool for high throughput sequence data. (2010).

44 Hartley, S. W. & Mullikin, J. C. QoRTs: a comprehensive toolset for quality control and data processing of RNA-Seq experiments. *BMC Bioinformatics* **16**, 224, doi:10.1186/s12859-015-0670-5 (2015).

45 Team, R. C. R: A Language and Environment for Statistical Computing. *R Foundation for Statistical Computing* (2017).

46 Wickham, H. *et al.* ggplot2: Elegant Graphics for Data Analysis. (2016).

47 Martin, M. Cutadapt removes adapter sequences from high-throughput sequencing reads. *EMBnet.journal* **17**, 10-12, doi:https://doi.org/10.14806/ej.17.1.200 (2011).

48 Dobin, A. *et al.* STAR: ultrafast universal RNA-seq aligner. *Bioinformatics* **29**, 15-21, doi:10.1093/bioinformatics/bts635 (2013).

49 Liao, Y., Smyth, G. K. & Shi, W. featureCounts: an efficient general purpose program for assigning sequence reads to genomic features. *Bioinformatics* **30**, 923-930, doi:10.1093/bioinformatics/btt656 (2014).

50 Love, M. I., Huber, W. & Anders, S. Moderated estimation of fold change and dispersion for RNA-seq data with DESeq2. *Genome Biol* **15**, 550, doi:10.1186/s13059-014-0550-8 (2014).

51 Li, H. & Durbin, R. Fast and accurate short read alignment with Burrows-Wheeler transform. *Bioinformatics* **25**, 1754-1760, doi:10.1093/bioinformatics/btp324 (2009).

52 Li, H. *et al.* The Sequence Alignment/Map format and SAMtools. *Bioinformatics* **25**, 2078-2079, doi:10.1093/bioinformatics/btp352 (2009).

53 Liu, T. Use model-based Analysis of ChIP-Seq (MACS) to analyze short reads generated by sequencing protein-DNA interactions in embryonic stem cells. *Methods in molecular biology* **1150**, 81-95, doi:10.1007/978-1-4939-0512-6_4 (2014).

54 Stark, R. & Brown, G. DiffBind: differential binding analysis of ChIP-Seq peak data. (2011).

55 Yu, G., Wang, L. G. & He, Q. Y. ChIPseeker: an R/Bioconductor package for ChIP peak annotation, comparison and visualization. *Bioinformatics* **31**, 2382-2383, doi:10.1093/bioinformatics/btv145 (2015).

56 BioconductorCoreTeam & BioconductorPackageMaintainer. TxDb.Mmusculus.UCSC.mm10.knownGene: Annotation package for TxDb object(s). *R package version 3.4.7.* (2019).
57 Leek, J. T. *et al.* sva: Surrogate Variable Analysis. *R package version 3.44.0*, doi:10.18129/B9.bioc.sva (2022).
58 Schep, A. N., Wu, B., Buenrostro, J. D. & Greenleaf, W. J. chromVAR: inferring transcription-factor-associated accessibility from single-cell epigenomic data. *Nature methods* **14**, 975-978, doi:10.1038/nmeth.4401 (2017).
59 Weirauch, M. T. *et al.* Determination and inference of eukaryotic transcription factor sequence specificity. *Cell* **158**, 1431-1443, doi:10.1016/j.cell.2014.08.009 (2014).
60 Ramirez, F. *et al.* deepTools2: a next generation web server for deep-sequencing data analysis. *Nucleic Acids Res* **44**, W160-165, doi:10.1093/nar/gkw257 (2016).
61 Carroll, T. & Barrows, D. profileplyr: Visualization and annotation of read signal over genomic ranges with profileplyr. *R package version 1.12.0.* (2022).
62 Gu, Z., Eils, R. & Schlesner, M. Complex heatmaps reveal patterns and correlations in multidimensional genomic data. *Bioinformatics* **32**, 2847-2849, doi:10.1093/bioinformatics/btw313 (2016).
63 Kuleshov, M. V. *et al.* Enrichr: a comprehensive gene set enrichment analysis web server 2016 update. *Nucleic Acids Res* **44**, W90-97, doi:10.1093/nar/gkw377 (2016).

Figure 1| TST undergo robust proliferation but do not gain effector function

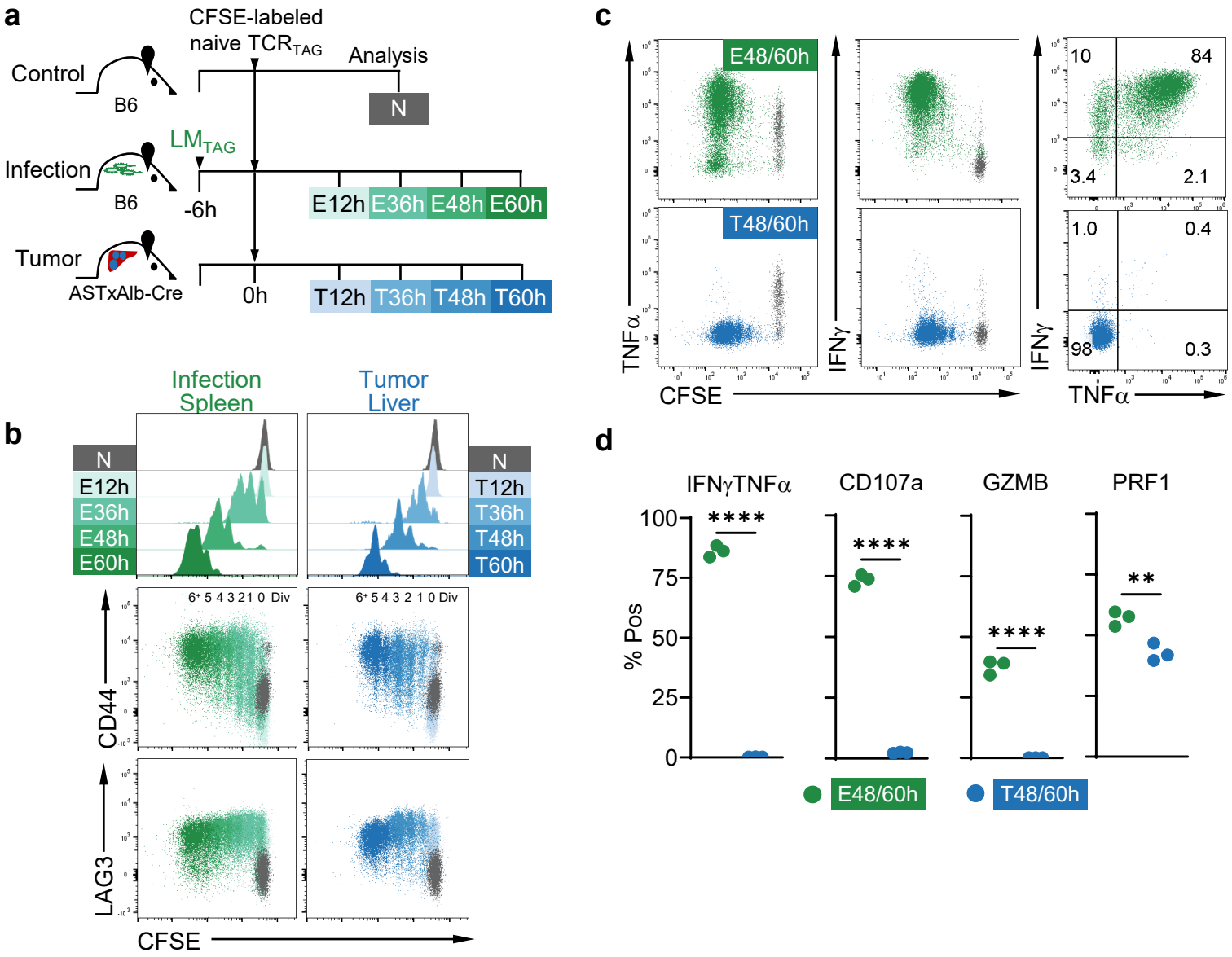

Figure 1| TST undergo robust proliferation but do not gain effector function. a, Experimental scheme: CFSE-labeled naive TCR_{TAG} (Thy1.1) were adoptively transferred into B6 (Thy1.2), LM_{TAG}-infected B6 (Thy1.2), or ASTxAlb-Cre mice (Thy1.2) bearing late-stage liver tumors. TCR_{TAG} were re-isolated at 12, 36, 48, and 60 hours (h) from infected spleen or tumor livers for flow cytometric analysis (Naive *in vivo* (N; grey); Effector (E; green); Tumor (T; blue)). **b**, TCR_{TAG} CFSE dilution assessed at each timepoint (upper) with CD44 and LAG3 versus CFSE dilution at all timepoints (lower) shown in comparison to N. All flow plots are gated on live $CD8^+$ $Thy1.1^+$ TCR_{TAG}, and data for each timepoint is concatenated from 3-4 biologic replicates. **c**, TCR_{TAG} IFNγ and TNFα production after 4h *ex vivo* TAG peptide stimulation, assessed by flow cytometry. Inset numbers represent percent of population in each gate. Gates were set based on no stimulation controls. **d**, Percentage of $IFN\gamma^+TNF\alpha^+$ and $CD107a^+$ $CD8^+$ $Thy1.1^+$ TCR_{TAG} (E48/60h and T48/60h) following *ex vivo* TAG peptide stimulation, and granzyme B (GZMB) and perforin (PRF1) expression immediately *ex vivo*. Each symbol represents an individual mouse. $^{**}P<0.01$, $^{****}P<0.0001$ determined using unpaired two-tailed Student's t-test. Experiments were repeated three times with n=3-4 for infection and tumor-bearing mice groups.

Figure 2| Tumor-induced TST dysfunction is established prior to cell division

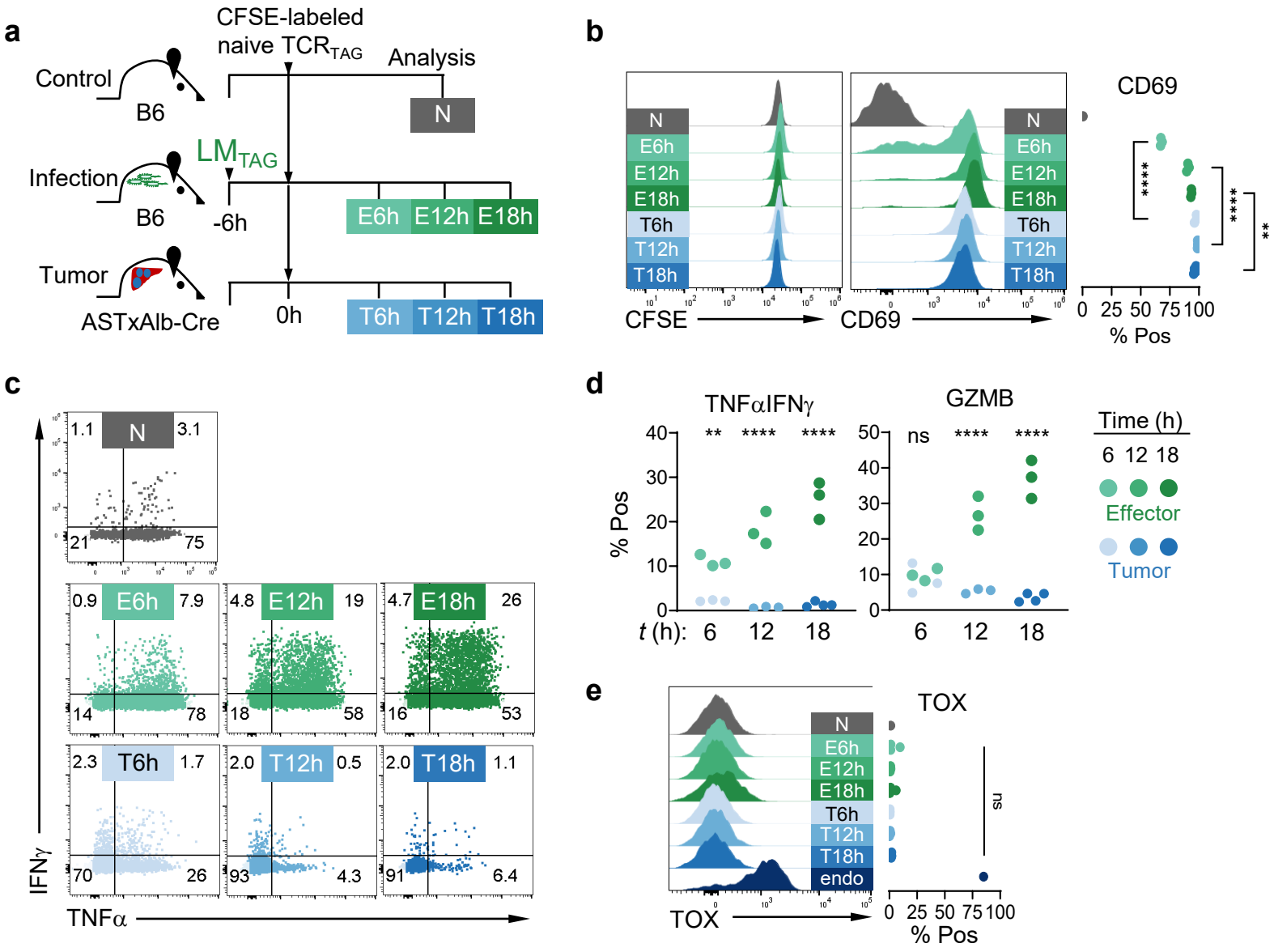

Figure 2| Tumor-induced TST dysfunction is established prior to cell division. a, Experimental scheme: CFSE-labeled naive TCR_{TAG} (Thy1.1) were adoptively transferred into B6 (Thy1.2), LM_{TAG}-infected B6 (Thy1.2), or ASTxAlb-Cre mice (Thy1.2) bearing late-stage liver tumors, and lymphocytes were re-isolated from tumor livers (blue) and infected spleens (green) at 6, 12, and 18h post-transfer for analysis by flow cytometry. **b**, Live $CD8^+$ $Thy1.1^+$ TCR_{TAG} CFSE dilution at each timepoint (left) and histogram and summary plot of CD69 expression (right) shown in comparison to naive *in vivo* (N; grey). **c**, TCR_{TAG} intracellular IFNγ and TNFα production after 4h *ex vivo* TAG peptide stimulation, with inset numbers indicating percentage of cells in each gate. Gates set based on no stim controls. **d**, Summary plots of TNFαIFNγ double-positive and *ex* vivo GZMB expression in TCR_{TAG}. Each symbol represents an individual mouse. **e**, Histograms and summary plots of TOX expression. $CD8^+$ $CD90.1^-$ $PD1^{hi}$ endogenous (endo) dysfunctional T cells are shown as the positive control for TOX staining. Histograms show representative data of group. $^{**}P<0.01$, $^{****}P<0.0001$ determined by two-way ANOVA with post hoc Tukey test. Experiments were repeated twice with n=3-4 mice per group.

Figure 3| Dysfunction-associated epigenetic programming is enacted prior to cell division

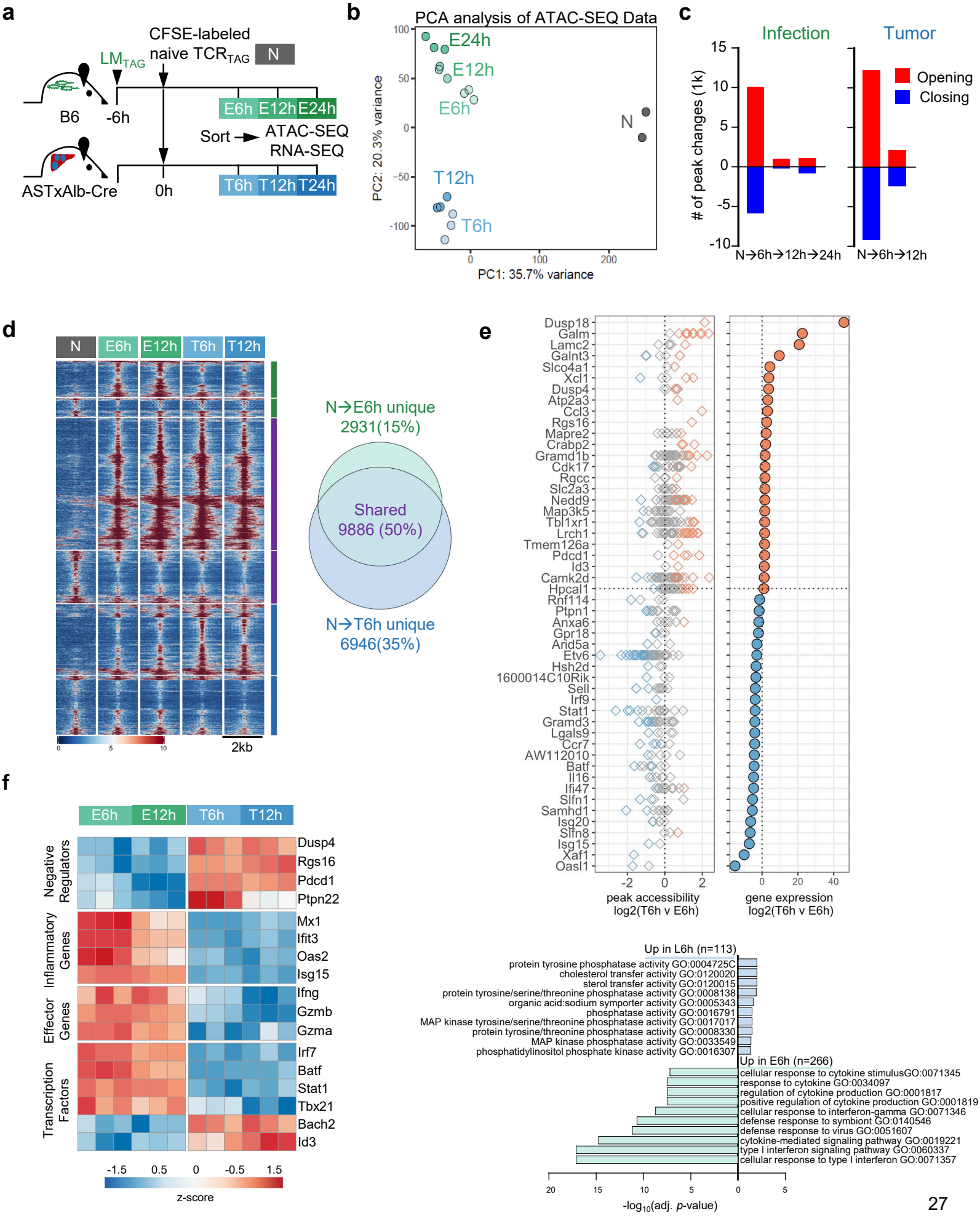

Figure 3| Dysfunction-associated epigenetic reprogramming is enacted prior to cell division. a, Experimental scheme. CFSE-labeled naive TCR_{TAG} (Thy1.1) were adoptively transferred into LM_{TAG}-infected B6 (Thy1.2), or ASTxAlb-Cre mice (Thy1.2) bearing late-stage liver tumors, and lymphocytes were flow-sorted from spleens and livers at 6, 12, and 24h post-transfer. **b**, Principal component analysis (PCA) comparing peak accessibility of naive (N; grey), and TCR_{TAG} differentiating during acute infection (green) and in tumors (blue) at 6, 12, and 24h post-transfer. Each symbol represents a single biological replicate. **c**, Number of chromatin accessibility peak changes during each transition (opening peaks, red; closing peaks, blue; *FDR*<0.05). **d**, Chromatin accessibility heatmap. Each row represents one of 19,763 differentially accessible peaks (*FDR*<0.05, |Log2FC| >1) displayed over 2kb window centered on the peak summit. Scale units are reads per genomic content (RPGC) normalized to 1x sequencing depth for 20 bp bins with blue indicating closed chromatin and red open chromatin. Peaks are ordered by membership within each subset shown in the Venn diagram (right) and hierarchical-clustering within the subset. Venn diagram showing quantity of differentially accessible chromatin peaks (DAC) that are unique to T cells in infection, unique to T cells in tumors, or shared between T cells in infection and tumors. **e,** Combined chromatin accessibility and differential gene expression analysis of TCR_{TAG} in tumor livers relative to infected spleens at 6h timepoint. Upper panel shows 50 most differentially-expressed genes (*FDR*< 0.05, |Log2FC| >1) with at least one DAC (*FDR*< 0.05). Each row of diamonds (left) corresponds to one gene and shows opening (red), unchanged (grey), and closed (blue) DAC. Circles (right) indicate corresponding gene expression (upregulated in red, downregulated in blue). Lower panel shows Gene ontology analysis performed on all DEG with at least one DAC in TCR_{TAG} in tumors relative to infection at 6h (113 genes up; 266 down). **f,** Heatmap showing differential gene expression between TCR_{TAG} in tumor versus infection at 6h from selected pathways (adjusted *P* <0.05, $|Log_2FC|$ >1), z-score normalization across rows.

Figure 4| Pre-division tumor-induced TST chromatin remodeling is reinforced with time and tumor antigen exposure

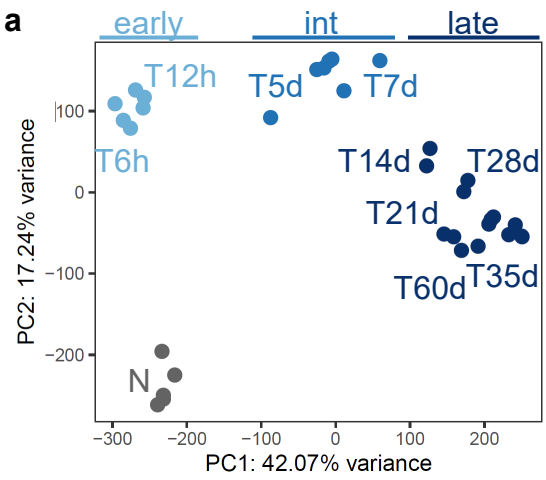

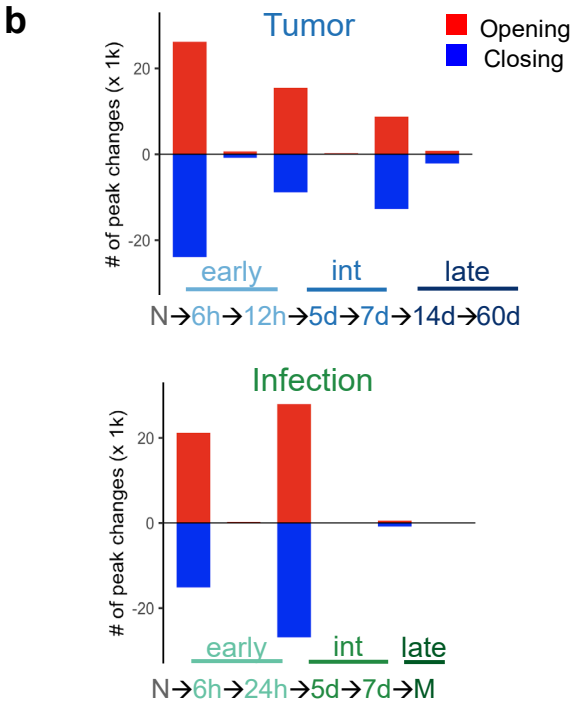

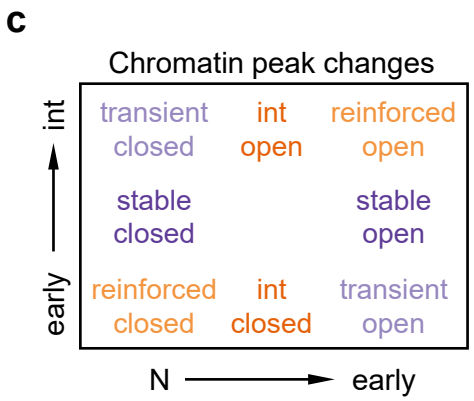

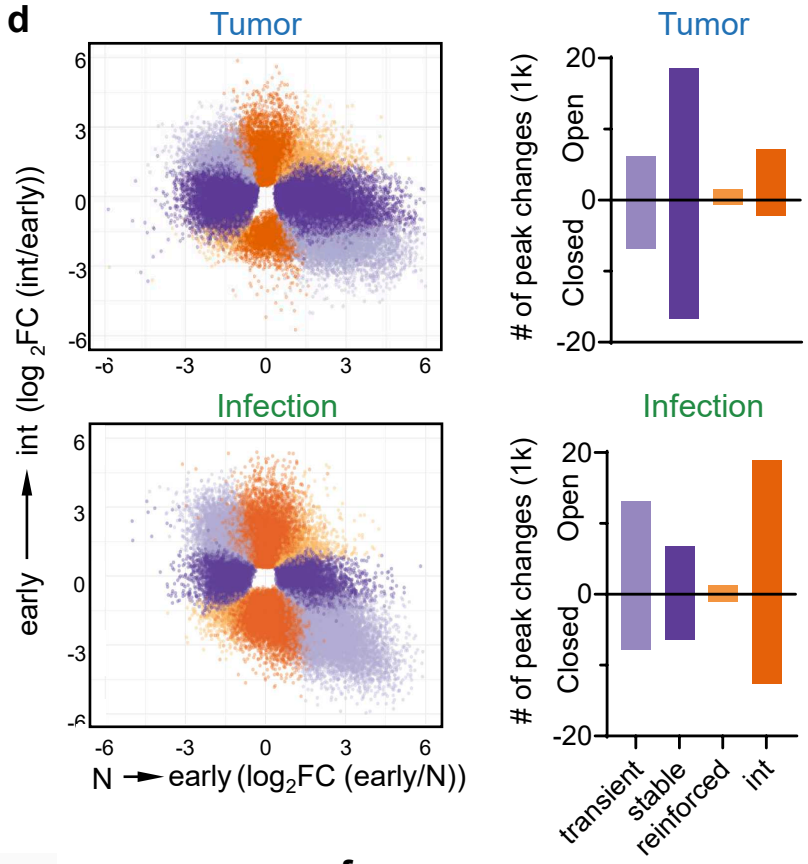

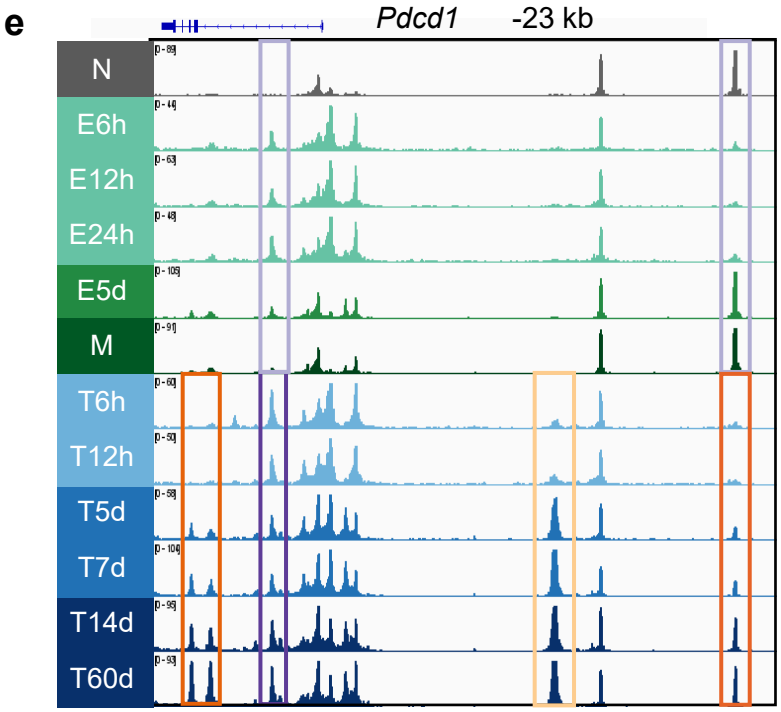

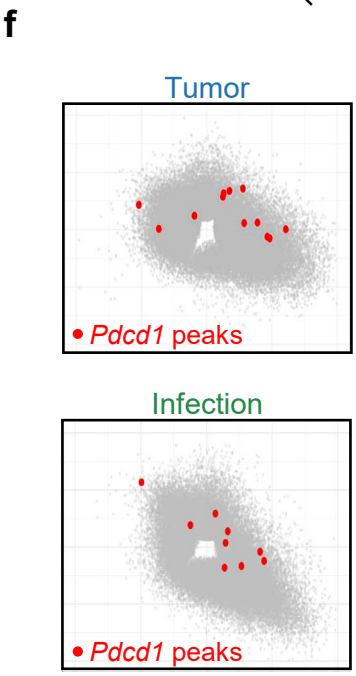

Figure 4| Pre-division tumor-induced TST chromatin remodeling is reinforced with time and tumor antigen exposure. a, PCA of chromatin accessibility of naive TCR_{TAG} (N) and after 6, 12h (early), 5d, 7d (intermediate; int), 14d, 21d, 28d, 35d, and 60d+ (late) in liver tumors. **b**, Number of chromatin accessibility peak changes during CD8 T cell differentiation in tumors (upper) and infection (lower) across each transition (opening peaks, red; closing peaks, blue) *FDR*<0.05). **c**, Legend corresponding to part d identifying chromatin accessibility peak quadrants in scatterplots of early transition peak accessibility changes (x-axis) versus later transition peak changes (y-axis)**. d,** Upper panel shows chromatin peak accessibility changes during naive (N) → early (T6h) transition (log2FC T6h/N) versus early → int (T5d) transition (log2FC T5d/T12h). Lower panel shows chromatin peak accessibility changes during N→ early (E6h) transition (log2FC E6h/N) versus early → int (E5d) transition (log2FC E5d/E24h). Each point represents an individual DAC peak colored according to the legend in c. To the right are shown corresponding bar plots showing the number of chromatin peaks in each quadrant with opening peaks above the axis and closing peaks below the axis (includes DAC with adjusted *P*<0.05 for either comparison). **e**, Chromatin accessibility profile across the *Pdcd1* locus for TCR_{TAG} differentiating during infection and in liver tumors. Boxes highlight differentially accessible peaks in tumor and/or infection colored as in c. The exhaustion-associated -23kb enhancer peak in *Pdcd1* is highlighted in light orange denoting a chromatin peak whose opening is reinforced during tumor progression. Light purple boxes highlight transiently closed and open peaks found in TCR_{TAG} during infection, while for TCR_{TAG} in tumors, the dark purple box highlights a peak that opens and is maintained at later timepoints, and the dark orange boxes highlight peaks that open early and increase in accessibility at later timepoints. **f**, Scatterplot highlighting individual *Pdcd1* peaks (red) in TCR_{TAG} in tumors and infected mice relative to the overall pattern of chromatin peak changes (grey).

Figure 5| Duration of tumor antigen exposure determines dysfunction stability and imprinting

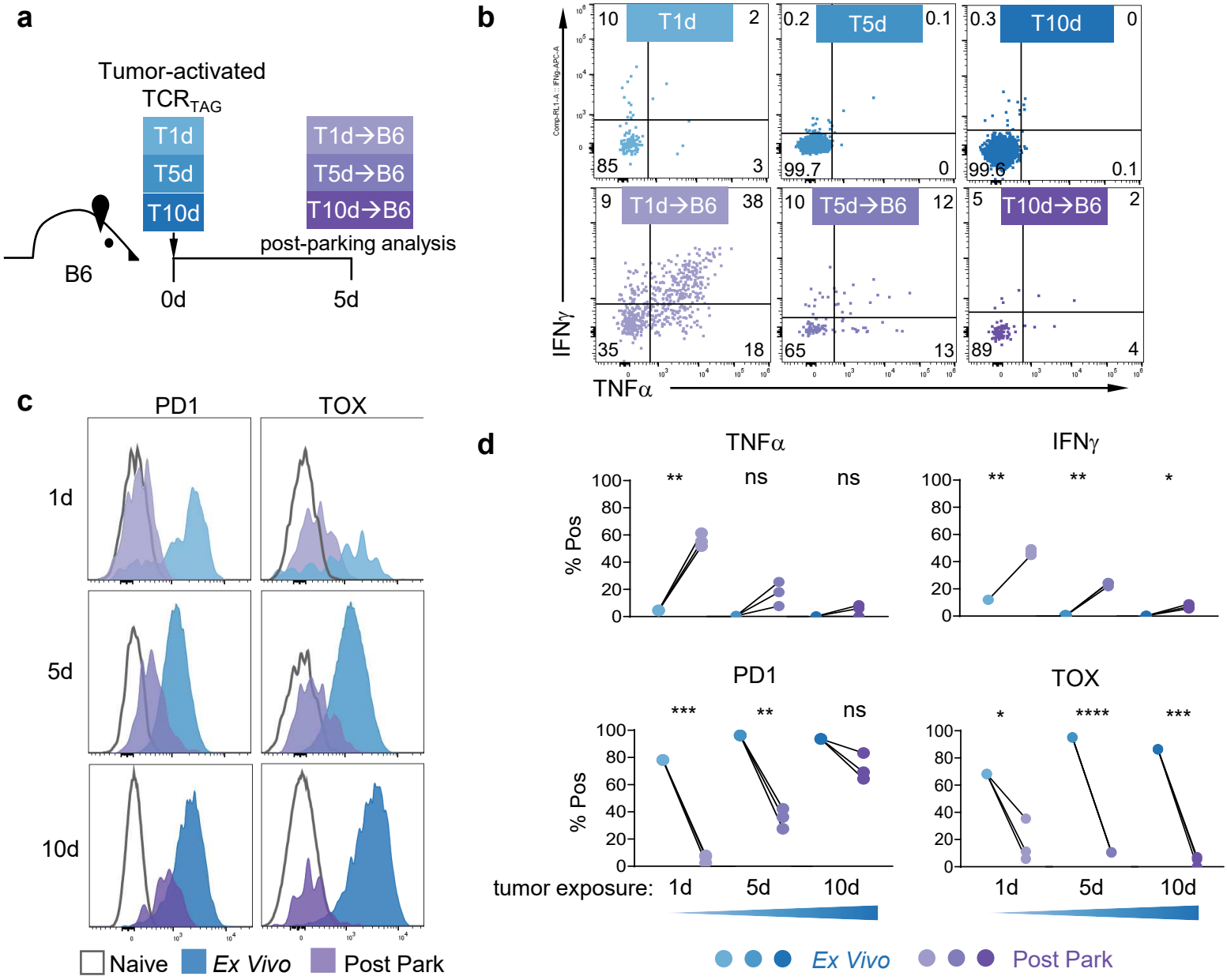

Figure 5| Duration of tumor antigen exposure determines dysfunction stability and imprinting. **a,** Experimental scheme: TCR_{TAG} activated in tumors for 1, 5, or 10d were isolated from tumors, transferred to tumor-free B6 mice, parked for 5d, and then isolated from secondary hosts and analyzed. **b,** Live $CD8^+$ $Thy1.1^+$ TCR_{TAG} analyzed *ex vivo* from tumors (upper) and after 5d parking (lower). TNFα and IFNγ production was measured following 4h *ex vivo* TAG peptide stim. Inset numbers represent percentage of population within each gate. Gates set based on no peptide stimulation controls. **c,** Histogram plots of *ex vivo* tumor activated TCR_{TAG} (blue) and concatenated post-parking samples (purple), with naive (N; grey) for comparison. TCR_{TAG} activated in tumors for 1d (upper), 5d (middle), and 10d (lower). **d,** Summary plots show the percentage positive for TNFα, IFNγ, PD1, and TOX *ex vivo* (for pooled donor TCR_{TAG} from 3-4 mice) and following 5d parking. **P*<0.05, ***P*<0.01, ****P*<0.001, *****P*<0.0001, ns=not significant, determined for change from baseline by one sample Student's t-test. Experiments were repeated twice with n=3-4 mice per group.

Extended Data Figure 1

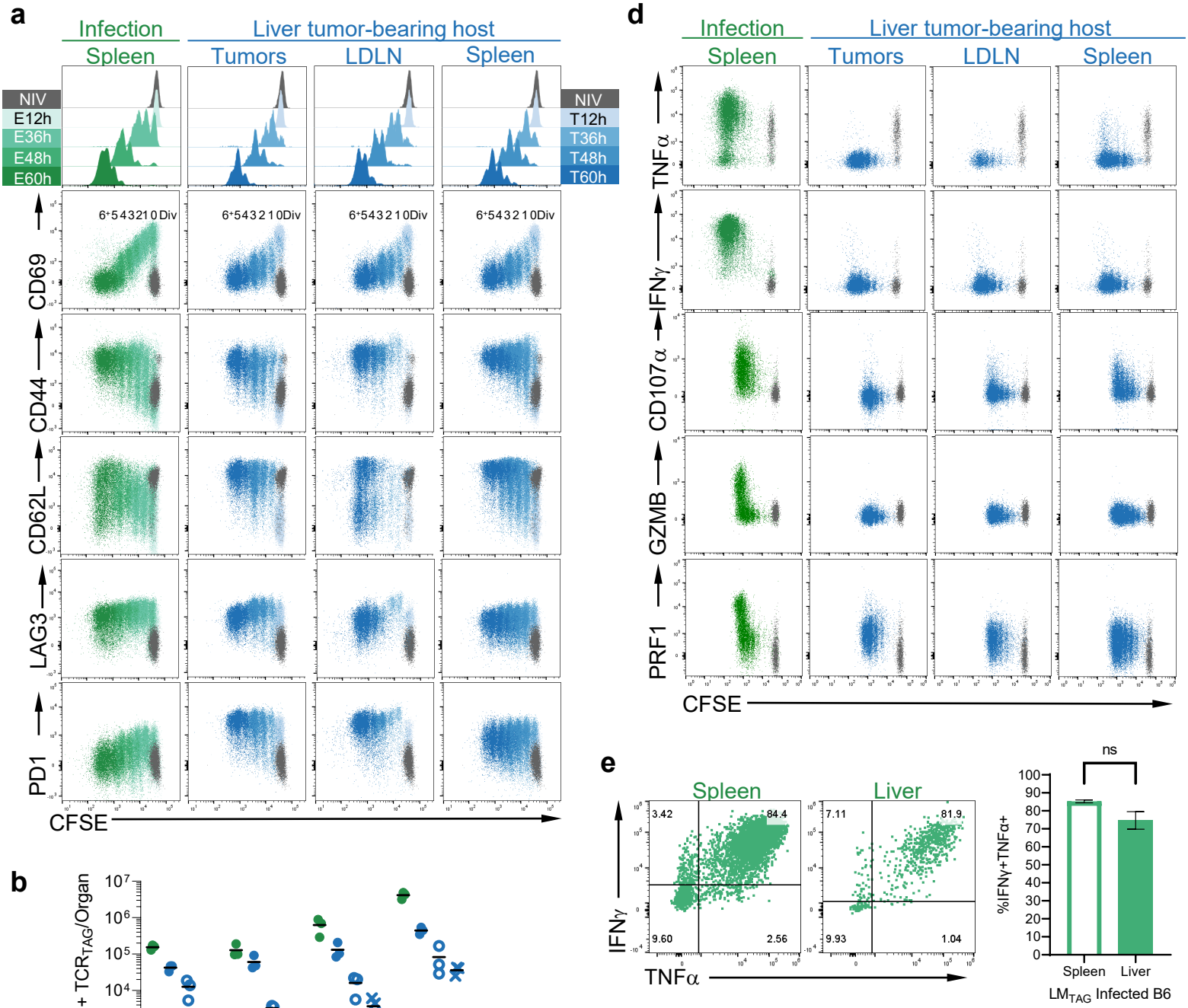

Extended Data Figure 1| a, Live $CD8^+$ $Thy1.1^+$ TCR_{TAG} CFSE dilution and expression of surface markers at each timepoint from LM_{TAG}-infected spleens (green) or for tumor-bearing mice (blue), from liver tumors, liver draining lymph nodes (LDLN), and spleens, shown relative to naive *in vivo* control (N; grey). Each timepoint is concatenated from 3-4 biologic replicates. **b,** Counts of TCR_{TAG} per organ; black bars represent population mean. **c,** TCR_{TAG} IFNγ and TNFα expression following 4h *ex vivo* peptide stim for 36h time point (divisions 1-3) in LM_{TAG}-infected spleens or tumor livers. **d,** TCR_{TAG} from pooled 48 and 60h timepoints. TNFα, IFNγ, and CD107a expression following 4h *ex vivo* TAG peptide stimulation. Granzyme B (GZMB) and perforin (PRF1) expression immediately *ex vivo* from infected or tumor bearing mice relative to N. **e,** TCR_{TAG} IFNγ and TNFα production at 48h timepoint in spleen and liver of infected mice following 4h *ex vivo* TAG peptide stim (left) and summary plot of percent $IFN\gamma^+TNF\alpha^+$ TCR_{TAG} (right). ns = not significant, determined by unpaired two-tailed Student's t-test.

Extended Data Figure 2

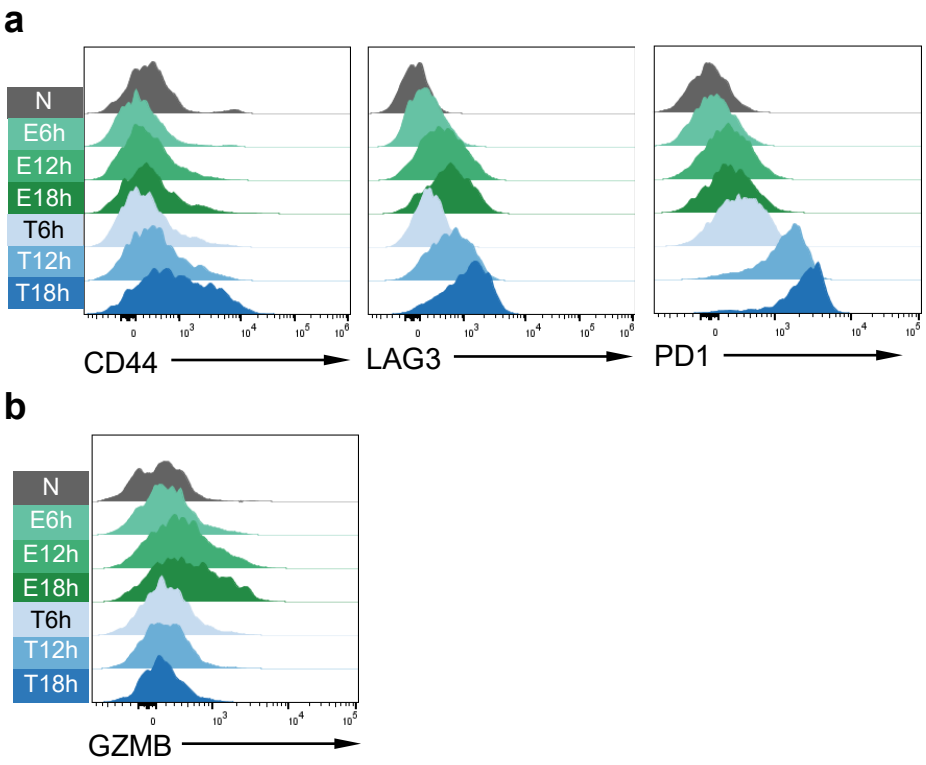

Extended Data Figure 2| Live $CD8^+$ $Thy1.1^+$ TCR_{TAG} analyzed from spleens of infected mice (green) and liver tumors from tumor-bearing hosts (blue) and at 6, 12, and 18h. **a,** Representative histograms of CD44, LAG3, and PD1 expression profiles. **b,** *Ex vivo* GZMB expression.

Extended Data Figure 3

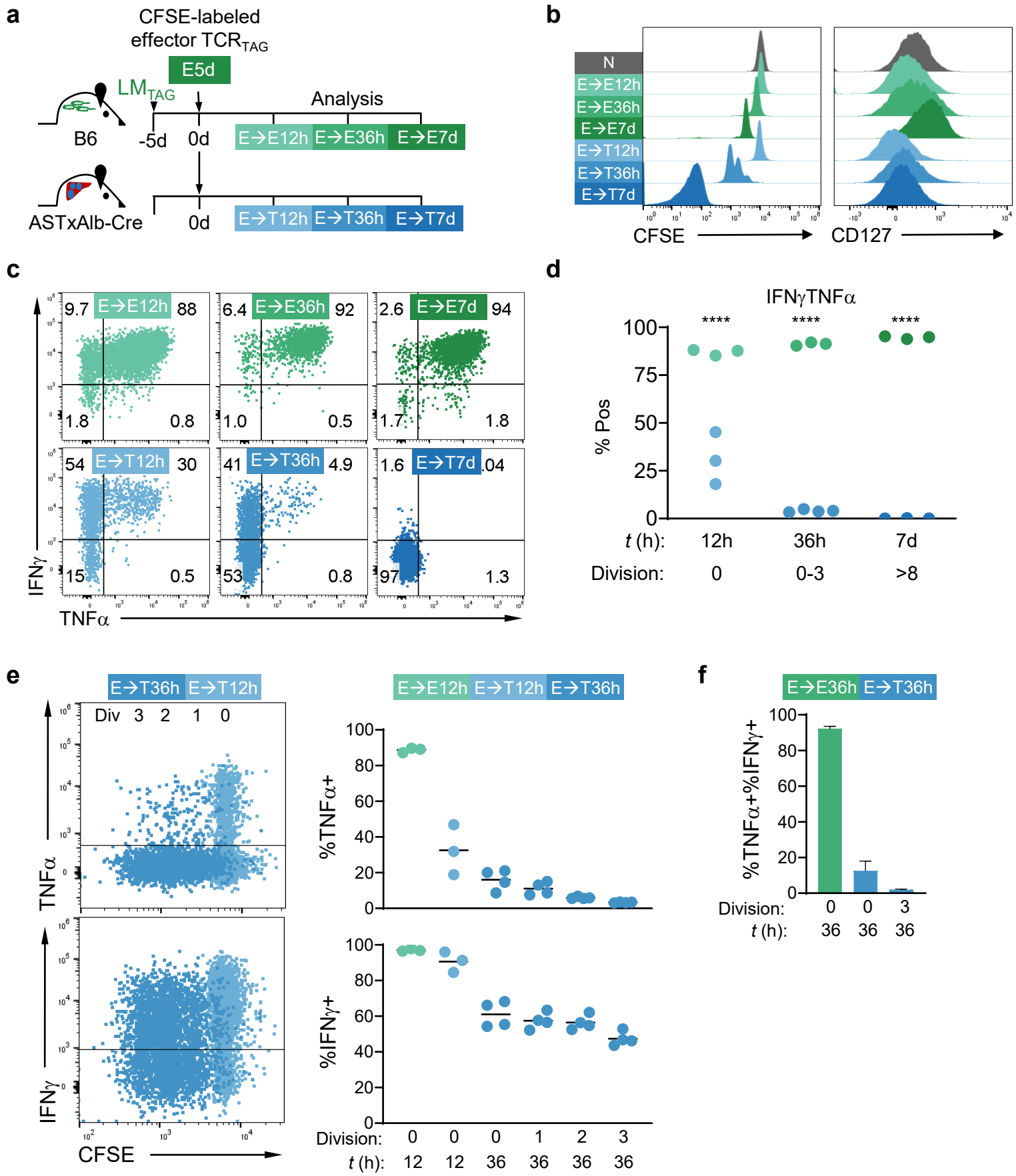

Extended Data Figure 3| a, Experimental scheme: committed effectors were generated by transferring naive TCR_{TAG} into LM_{TAG}-infected B6 mice and harvesting splenocytes 5 days (d) post transfer (E5d). E5d were CFSE-labeled and transferred into time-matched infected mice or tumor-bearing mice. TCR_{TAG} were re-isolated from infected spleens (green) or tumor livers (blue) of secondary recipients 12h, 36h, and 7d post-transfer. All flow plots are gated on live $CD8^+$ $Thy1.1^+$ cells. **b**, CFSE dilution and CD127 expression with naive TCR_{TAG} (N; grey) shown for comparison. **c**, TCR_{TAG} IFNγ and TNFα production after 4h *ex vivo* TAG peptide stimulation, with inset numbers indicating percentage of cells in each gate. Gates set based on no peptide stimulation controls. **d**, Summary plots of TNFαIFNγ double-positive TCR_{TAG}. Each symbol represents an individual mouse. **e**, Overlay of concatenated 12 and 36h timepoints from tumor livers showing TCR_{TAG} CFSE dilution and TNFα and IFNγ production following 4h TAG peptide stimulation (left). Summary plots of TNFα and IFNγ production (right) where each symbol represents a single mouse. **f,** Summary plot of IFNγTNFα double-positive TCR_{TAG} by cell division 36h post-transfer. ****P<0.0001 determined by two-way ANOVA with post-hoc Tukey test. Experiments were repeated three times with n=3-4 mice per group.

Extended Data Figure 4

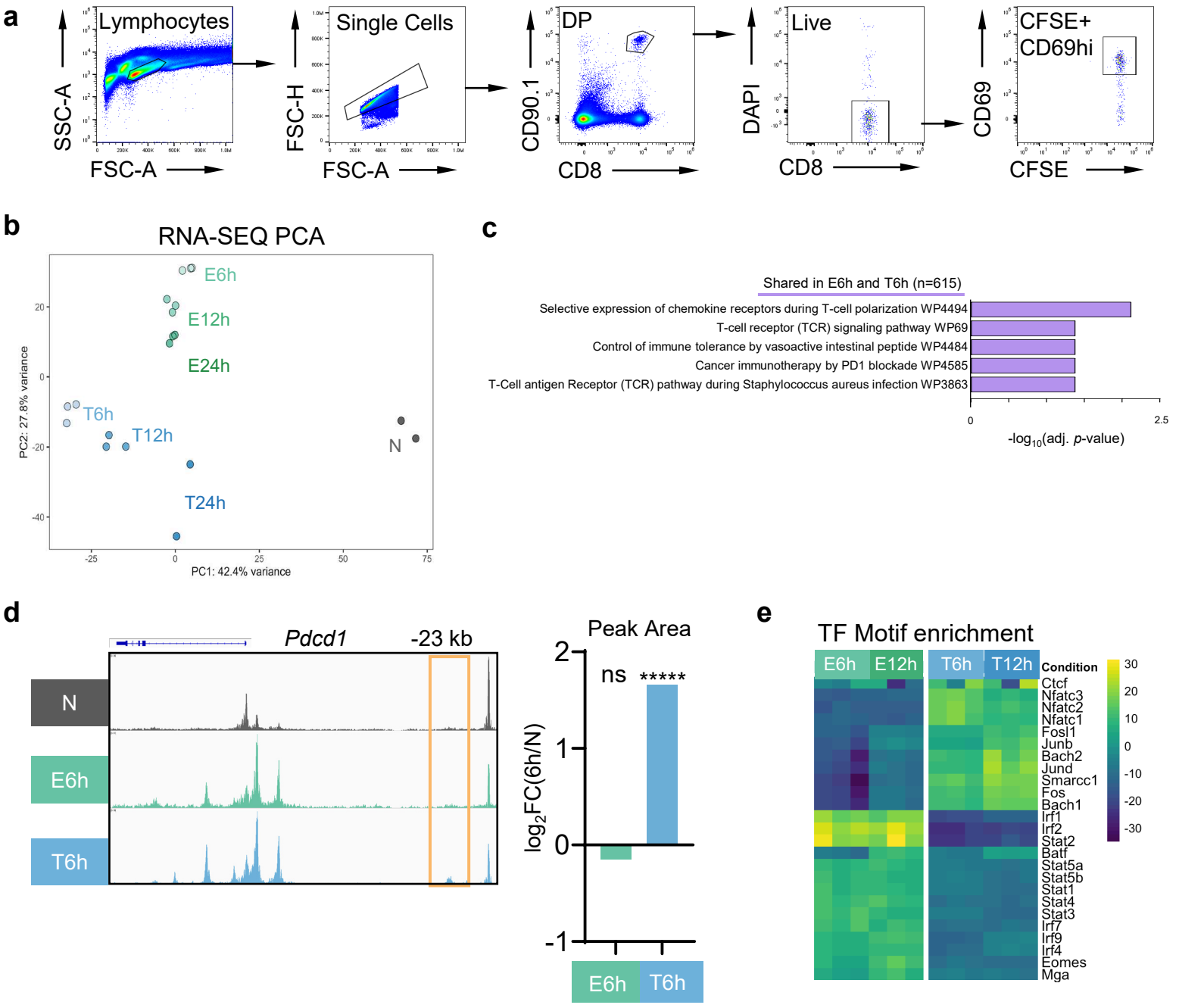

Extended Data Figure 4| a, Gating strategy to sort TCR_{TAG} from infected spleens or tumor livers for sequencing studies. **b,** Principal component analysis (PCA) of RNA-SEQ data comparing top 500 most variable genes between naive (N; grey) and TCR_{TAG} differentiating during acute infection (green) and in tumors (blue) at 6, 12, 24h post-transfer. Each symbol represents a single biological replicate. **c,** Pathway analysis was performed on genes with shared DAC found in TCR_{TAG} at 6h in infection and tumor compared to naive (Venn diagram in Fig. 3d). **d,** Chromatin accessibility profile across the *Pdcd1* locus with the exhaustion-associated -23kb enhancer highlighted in light orange (left). Summary plot of Log_2FC chromatin accessibility at the -23kb enhancer peak for E6h or T6h as compared to naive (N) (ns; not significant; ****$P<1.5x10^{-5}$**) e,** Heatmap of chromVAR computed deviations z-score for the top 25 most variable transcription factor (TF) motifs across TCR_{TAG} tumor and infection at 6 and 12h.

Extended Data Figure 5

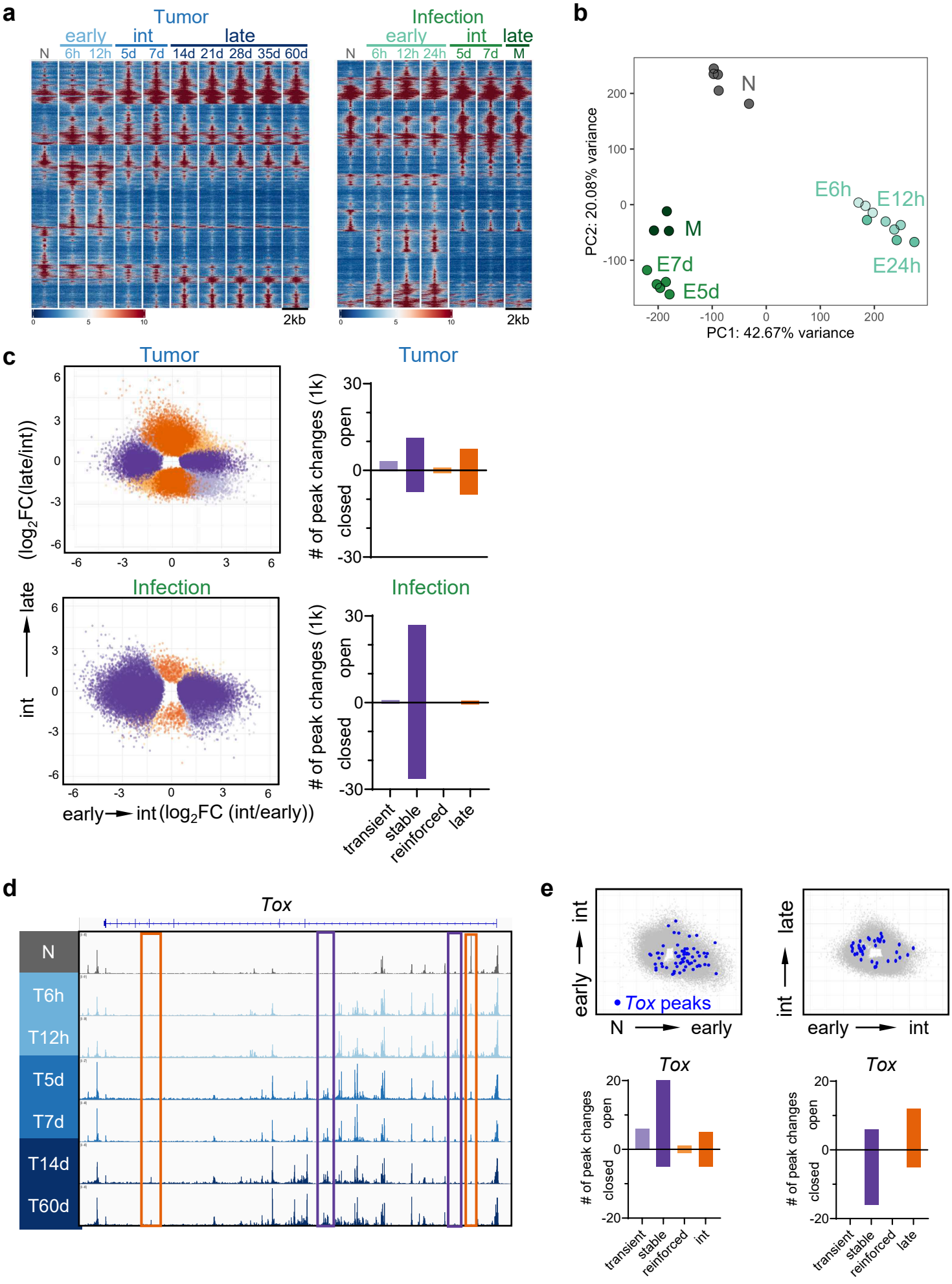

Extended Data Figure 5| a, Chromatin accessibility heatmap showing naive (N) and TCR_{TAG} from 6h to 60+d in liver tumors of ASTxAlb-Cre mice (left) and 6h to 60+d memory (M) in LM_{TAG}-infected mice (right). Each row represents one of 55,563 (left) or 56,057 (right) differentially accessible peaks (DAC) (differentially accessible between at least one sequential timepoint comparison; adjusted P <0.05, $|Log_2FC|$ >1) displayed over 2kb window centered on the peak summit. Scale units are RPGC normalized to 1x sequencing depth for 20 bp bins with blue indicating closed chromatin and red open chromatin. Peaks are clustered by k-means (k=6). **b,** PCA comparing chromatin accessibility of TCR_{TAG} from 6h to M during infection. Each symbol represents a single biological replicate. **c,** Upper panel shows chromatin peak accessibility changes for early (T12h) → intermediate (T5d) transition (log2FC T5d/12h) versus int (T7d) → late (T14d) transition (log2FC T14d/T7d) (upper). Lower panel shows chromatin peak accessibility changes for early (E24h) → int (E5d) transition (log2FC E5d/E24h) versus int (E7d) → late (M) transition (log2FC M/E7d). Each point represents an individual DAC peak colored according to the scheme in Fig. 4c. To the right are shown corresponding bar plots showing the number of chromatin peaks in each sector with opening peaks above the axis and closing peaks below the axis (includes DAC with adjusted P<0.05 for either comparison). **d,** Chromatin accessibility profile across the *Tox* locus for TCR_{TAG} differentiating in liver tumors. The dark orange boxes highlight *Tox* peaks that opened or closed during the late T7d → T14d transition, while the dark purple boxes highlight peaks that opened or closed during the int T12h → T5d transition and were maintained during the later transition. **e,** Scatterplot highlighting individual *Tox* peaks (blue) in TCR_{TAG} in tumors during the N → early versus early → int transitions (upper left) and the early → int versus int → late transitions (upper right). Below are the corresponding bar plots showing the number of *Tox* chromatin peaks in each sector with peaks opening above the axis and peaks below the axis closing (includes DAC with adjusted P<0.05 for either comparison).